

PS-CAD: Local Geometry Guidance via Prompting and Selection for CAD Reconstruction

BINGCHEN YANG, HAIYONG JIANG, HAO PAN, PETER WONKA, JUN XIAO, and GUOSHENG LIN

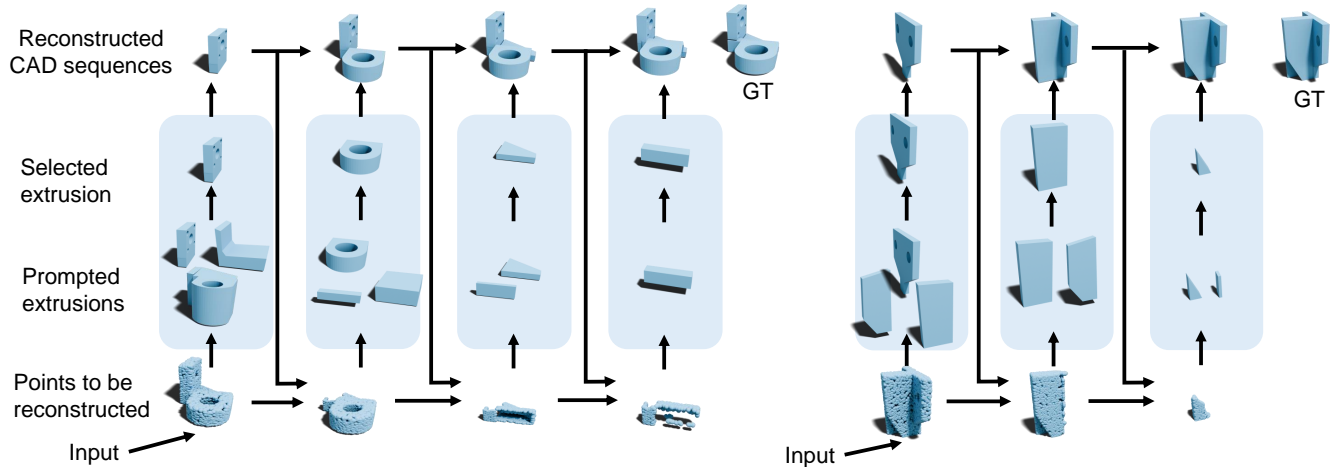


Fig. 1. Two examples for the iterative PS-CAD reconstruction. PS-CAD takes a point cloud as input (bottom left labeled input) and produces a CAD modeling sequence (the top row) using an iterative reconstruction architecture. For each iteration (one column in the figure), the method first determines a point cloud highlighting the parts that still need the most work (bottom row labeled points to be reconstructed). Then we extract planar prompts to guide the estimation of extrusion cylinders (middle labeled prompted extrusions). After that, the method selects the most suitable one (middle labeled selected extrusion). The top shows the reconstructed CAD sequence step by step. This process iterates until the final shape is reconstructed.

Reverse engineering CAD models from raw geometry is a classic but challenging research problem. In particular, reconstructing the CAD modeling sequence from point clouds provides great interpretability and convenience for editing. Analyzing previous work, we observed that a CAD modeling sequence represented by tokens and processed by a generative model, does not have an immediate geometric interpretation. To improve upon this problem, we introduce geometric guidance into the reconstruction network. Our proposed model, PS-CAD, reconstructs the CAD modeling sequence one step at a time as illustrated in Fig. 1. At each step, we provide two forms of geometric guidance. First, we provide the geometry of surfaces where the current reconstruction differs from the complete model as a point cloud. This helps the framework to focus on regions that still need work. Second, we use geometric analysis to extract a set of planar prompts, that correspond to candidate surfaces where a CAD extrusion step could be started. Our framework has three major components. Geometric guidance computation extracts the two types of geometric guidance. Single-step reconstruction computes a single candidate CAD modeling step for each provided prompt. Single-step selection selects among the candidate CAD modeling steps. The process continues until the reconstruction is completed. Our quantitative results show a significant improvement across all metrics. For example, on the dataset DeepCAD, PS-CAD improves upon the best published SOTA method by reducing the geometry errors (CD and HD) by 10%, and the structural error (ECD metric) by about 15%.

Authors' address: Bingchen Yang; Haiyong Jiang; Hao Pan; Peter Wonka; Jun Xiao; Guosheng Lin.

© 2024 Association for Computing Machinery.
This is the author's version of the work. It is posted here for your personal use. Not for redistribution. The definitive Version of Record was published in , <https://doi.org/10.1145/nnnnnnnn.nnnnnnnn>.

CCS Concepts: • **Computing methodologies** → **Shape modeling; Neural networks.**

Additional Key Words and Phrases: CAD reconstruction, promptable, sequence reconstruction

ACM Reference Format:

Bingchen Yang, Haiyong Jiang, Hao Pan, Peter Wonka, Jun Xiao, and Guosheng Lin. 2024. PS-CAD: Local Geometry Guidance via Prompting and Selection for CAD Reconstruction. 1, 1 (May 2024), 18 pages. <https://doi.org/10.1145/nnnnnnnn.nnnnnnnn>

1 INTRODUCTION

Reconstructing Computer-Aided Design (CAD) models from scans is one of the long-sought goals in geometric modeling and plays a critical role in reverse engineering. In addition to 3D surface details, CAD models also capture the structure of the 3D models which facilitates 3D editing.

Many endeavors have been devoted to this problem. Some approximate an object with a set of parametric primitives with a focus on shape abstraction [Li et al. 2019; Paschalidou et al. 2019; Tulsiani et al. 2017; Yan et al. 2021] or detail preservation [Guo et al. 2022b; Li et al. 2023b; Wang et al. 2020; Zhu et al. 2023]. However, simply assembling parametric primitives provides only the surface and boundary information of the shape. These approaches do not capture the structure of the CAD model encoded by modeling operations. To this end, Constructive Solid Geometry (CSG)-based representations [Ellis et al. 2019; Jones et al. 2022; Kania et al. 2020; Ren et al. 2021, 2022; Sharma et al. 2018, 2022; Yu et al. 2023, 2022] are explored for their

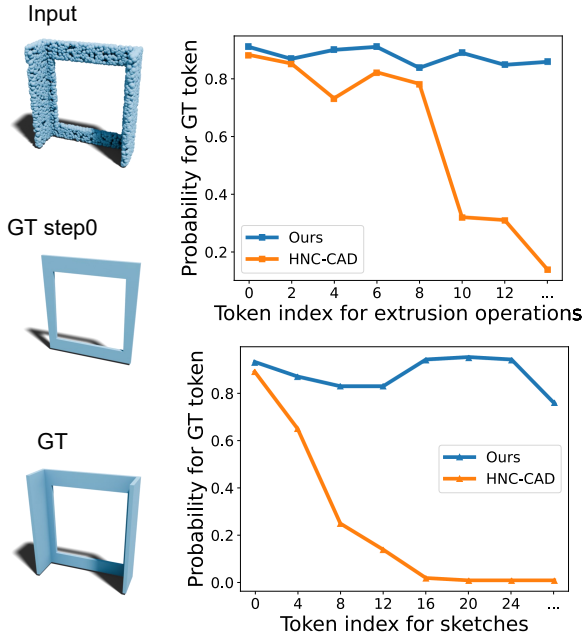


Fig. 2. Token probabilities for our method and HNC-CAD [Xu et al. 2023]. Left: the input point cloud, the first CAD modeling step of the ground-truth, and the final output of the ground truth. Right: Probabilities of the ground truth tokens for sketches and extrusion operations for HNC-CAD and our method. Our method performs stably for each token while for HNC-CAD the probabilities drastically decrease after generating several tokens.

explicit modeling steps. Another line of works [Khan et al. 2024; Lambourne et al. 2022; Li et al. 2023a; Ma et al. 2023; Uy et al. 2022; Wu et al. 2021] take a step further and directly learn to estimate a CAD modeling sequences from an input CAD model. These works decompose a CAD model into a list of CAD modeling steps. In our work, we adopt a domain-specific language (DSL) for CAD [Xu et al. 2022], where a CAD modeling step consists of a sketch (a 2D curve), an extrusion, and a Boolean operation (union or subtraction). The 3D shape defined by a 2D sketch and extrusion is called an extrusion cylinder. Even though previous work may have some slight deviations from this model, we use it as a common framework to structure the discussion of existing literature. There are two types of architectures used in previous work to tackle this problem. The first architecture is to generate CAD models using a feed-forward network (See Fig. 3-a, e.g. [Lambourne et al. 2022; Li et al. 2023a; Ma et al. 2023; Uy et al. 2022; Wu et al. 2021]). The feed-forward network predicts a fixed number of extrusion cylinders and Boolean operations jointly all at once, thus lacking the flexibility to adapt to input geometry with a varying number of CAD modeling steps and to sample different CAD modeling designs. The second architecture is to sequentially generate a CAD sequence using an auto-regressive deep learning model. (See Fig. 3-b, e.g. [Khan et al. 2024; Xu et al. 2023, 2022]). This model generates a CAD model one token at a time. A sequence of tokens (about 20 - 80) yields a single CAD modeling step. As each token does not have a special geometric meaning, this scheme does not consider local geometric contexts and results in

a rapid descent in the softmax probability of the sampled tokens, indicating inaccurate token sampling during CAD reconstruction (See Fig. 2). We further evolve this approach to yield a third type of architecture, generating a sequence one CAD modeling step at one time (See Fig. 3-c). We call this a prompt-and-select architecture. Each iteration of our framework outputs a single CAD modeling step and consists of three components: a) geometric guidance computation, b) single-step reconstruction, and c) single-step selection. We visualize the two previous network architectures and our proposed framework in Fig. 3. Step-wise CAD reconstruction is shown in Fig. 1.

This enables us to improve upon existing auto-regressive models by providing local geometric guidance. An auto-regressive model obtains the current state as a sequence of already-generated tokens. This sequence of tokens has no immediate geometric interpretation and this requires a lot of processing to obtain a geometric interpretation before the model can reason about which token to output next. We propose to provide three types of local geometric guidance for the auto-regressive model to improve its functionality. First, we provide the difference between the current reconstruction and the input model as point cloud. This let's the model know which parts it should focus on. Second, we geometrically analyze the model to find candidate planes from which a new CAD modeling step can be started. We then provide these candidate planes as input in the form of prompts, analog to segmentation prompts popular in recent work [Kirillov et al. 2023]. This provides the context for generating the next candidate CAD modeling step and the generated sketches (curves) are encouraged to lie on the prompt planes. Third, we implement a geometric form of lookahead sampling. Instead of simply sampling one token at a time based on the computed probability, we generate multiple complete candidate CAD modeling steps (each encoded as a sequence of tokens) and then evaluate the candidates to choose the most suitable one. The network trained for this component is supervised with geometric criteria. Fig. 1 shows how the proposed modeling pipeline builds a CAD model step by step. Fig. 3-c shows the proposed network architecture.

Our main contributions are:

- We propose an iterative prompt-and-select architecture to progressively reconstruct the CAD modeling sequence of a target shape.
- We propose the concept of local geometric guidance for auto-regressive models and propose three ways to integrate this guidance into the auto-regressive framework.
- Quantitative experiments demonstrate a significant improvement over the current state of the art. For example, on the dataset DeepCAD, our framework PS-CAD improves upon the best published SOTA method by reducing the geometry errors (CD and HD) by 10%, and the structural error (ECD) by about 15%.

2 RELATED WORK

In this section, we review related works on 3D CAD reconstruction with different output formats, ranging from parametric primitives, and CSG trees, to the CAD modeling sequence.

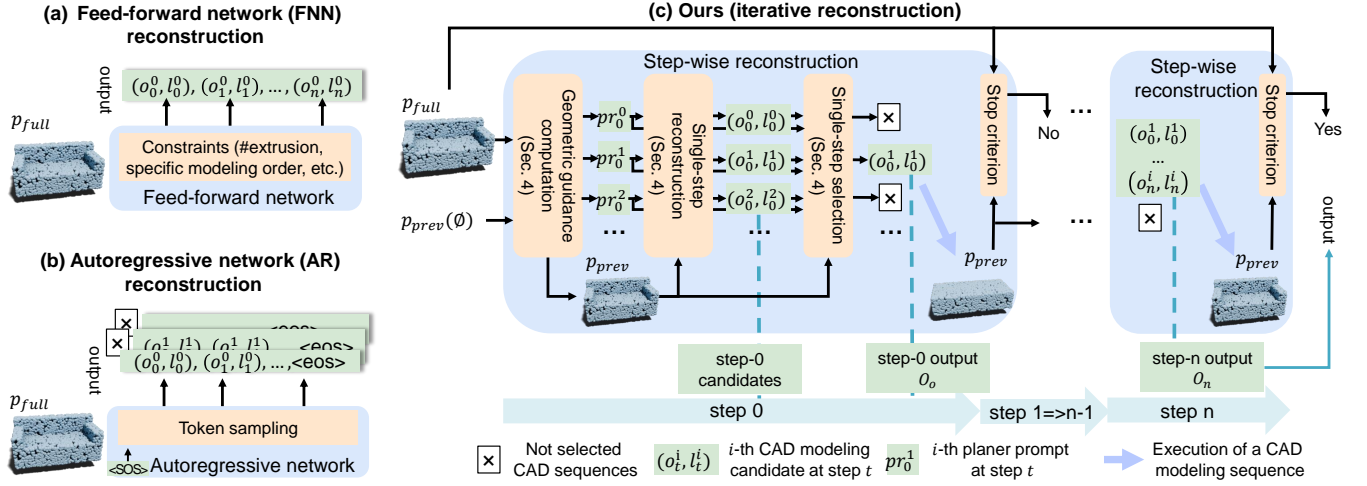


Fig. 3. Comparison of different reconstruction pipelines: (a) feed-forward network (FFN), (b) autoregressive network (AR), and (c) our iterative reconstruction. In (a), the FFN decomposes an input point cloud into a fixed number of extrusion cylinders and their Boolean operations, each of which is represented with a CAD modeling step (o_t^0, l_t^0) . In (b), the AR reconstructs the CAD modeling sequence token-by-token. By sampling different tokens without specific geometric meaning, the AR can reconstruct multiple CAD modeling sequences and output the one with the lowest reconstruction error. In (c), we propose an iterative pipeline with each iterative step consisting of three components: geometric guidance computation, single-step reconstruction, and single-step selection. At step t , the geometric guidance computation generates candidate prompts pr_t^i (in the form of sampled planes) and local geometric information p_{ref} to provide geometric guidance to the single-step reconstruction module. The single-step reconstruction module produces one candidate CAD modeling step (o_t^i, l_t^i) . Then, the single-step sequence selection module selects the CAD modeling step with the highest scores and concatenates the corresponding tokens to the output sequence. This process iterates n steps until a stop criterion is satisfied.

CAD Primitive Reconstruction. Most approaches in the scheme represent an input 3D shape as a set of parametric primitives to be assembled, where the parametric primitives can be edges, surface patches, 3D solids, etc. Traditional approaches first segment and fit an input shape with basic parametric primitives (e.g. planes, spheres, and cylinders) [Fish et al. 2014; Kim et al. 2013; Schnabel et al. 2007]. Recent advances in learning-based methods have improved the robustness of primitive fitting approaches [Li et al. 2019; Tulsiani et al. 2017; Yan et al. 2021] by being tolerable to outliers, meanwhile allowing for a wider variety of primitives for enhanced shape representation and better performance, including e.g. super quadratics [Paschalidou et al. 2019], convexes [Deng et al. 2020], learnable Bézier [Fu et al. 2023] and B-spline patches [Sharma et al. 2020], implicit fields [Park et al. 2019], etc. Another category of approaches [Guo et al. 2022b; Li et al. 2023b; Wang et al. 2020; Zhu et al. 2023] emphasize the preservation of sharp geometric features and learn to fit edges, corners that have a parity relation with surface patches from the input. Though these works can produce high-quality geometry, their results are mainly primitives missing the high-level CAD modeling operations, and therefore not easy to apply further editing.

CSG-tree based CAD Reconstruction. Pioneering works [Buchele and Crawford 2004; Fayolle and Pasko 2016; Hamza and Saitou 2004; Shapiro and Vossler 1991, 1993] investigate to express input 3D shape as Constructive Solid Geometry (CSG) [Laidlaw et al. 1986] with Boolean operations, well maintaining the shape construction information without loss of expressiveness. Typically, search-based

algorithms and pruning strategies are applied to build CSG trees [Du et al. 2018; Wu et al. 2018]. For learning-based CSG reconstruction, the key challenge is to combine the indifferentiable CSG tree construction with differentiable primitive fitting. Previous works address this problem by using reinforcement learning [Ellis et al. 2019; Jones et al. 2022; Sharma et al. 2018, 2022], recursive constructions based on hand-crafted geometric rules [Guo et al. 2022a], and novel learnable Boolean layers [Kania et al. 2020]. Successive approaches specify the CSG trees with fixed order and depth [Ren et al. 2021, 2022], together with dedicated differentiable objectives and networks [Yu et al. 2023, 2022]. However, to replicate the overall structure and retain fine geometric details with a fixed set of primitives, the structures of composed intermediate parts are seldom considered and therefore less interpretable and editable.

CAD Modeling sequence Reconstruction. To accommodate the modern CAD design pipeline, several approaches predict a CAD modeling sequence from a 3D CAD model. DeepCAD [Wu et al. 2021] encodes CAD modeling sequences as CAD domain-specific language (DSL) sequences and trains a transformer model conditioned on input to generate or reconstruct CAD DSL sequences directly. ZoneGraph [Xu et al. 2021] employs a zone graph to represent the CAD model given as B-rep. A zone corresponds to a 3D entity derived from the B-rep faces. In this way, predicting the CAD modeling sequence turns into a combinatorial problem in the discrete space permitted by the zone graph. Leveraging well-annotated datasets [Willis et al. 2021; Wu et al. 2021], Point2Cyl [Uy et al. 2022] derives a set of parametric extrusion cylinders with a specified set

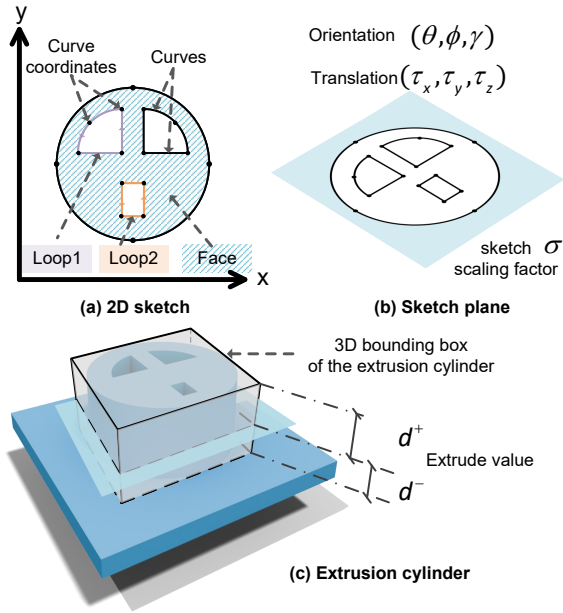


Fig. 4. Illustration for the sketch and extrude representation. a) We show a 2D sketch consisting of four loops (three inner loops and one outer loop). The four loops define a face shaded in blue. Each of the loops consists of one or multiple curves, where each curve is a linear segment (defined by two points), an arc (defined by three points), or a circle (defined by four points). The outer loop is an example of a circle. This example shows a single face, but in general, a sketch with multiple faces is also allowed. b) The 2D sketch is transformed from its local 2D coordinate system to the 3D coordinate system of the CAD model by translation, orientation, and scaling. c) The 2D sketch is extruded from a height d^- to a height d^+ defining an extrusion cylinder. We also use the bounding box of the extrusion cylinder in our computation.

size, based on segmentation of input shape. Lambourne et al. [2022] train a network to predict sketches and extruded values with a predefined CAD modeling sequence template. SECAD-Net [Li et al. 2023a] reconstructs parametric extrusions and combines them as the input CAD model using Union operation. The closest work to ours is the concurrent CAD-SIGNet [Khan et al. 2024]. It reconstructs the CAD modeling sequence using an autoregressive network. As the core design, it uses predicted extrusion operation to assist in predicting the sketch. Our approach has the following differences from CAD-SIGNet: (1) We iteratively reconstruct the CAD modeling steps that splice to the complete CAD modeling sequence, rather than output the complete CAD modeling sequence (see Fig. 3 (b) and (c) for comparison); (2) In each step we reconstruct multiple candidate CAD modeling steps based on prompts rather than token sampling (3) We devise a single-step selection module to select the best-fitted candidate, rather than rely on geometric criteria for CAD modeling sequence selection.

3 OVERVIEW

In this section, we first introduce the domain-specific language (DSL) used for encoding CAD modeling sequences in this paper. Then we

give an overview of our approach. Our approach takes a 3D CAD model given as point cloud as input and outputs a DSL sequence.

3.1 Preliminaries on the CAD DSL

We use the CAD DSL from SkexGen [Xu et al. 2022]. It decomposes a 3D CAD model into a sequence of CAD modeling steps (o_t, l_t) , where o_t is an *extrusion cylinder* and l_t is a *Boolean operation* (union or subtraction). An extrusion cylinder consists of a 2D sketch s_t and an extrusion operation e_t . The CAD modeling sequence O is a sequence of CAD modeling steps:

$$O = [(o_t, l_t)], \text{ where } o_t = (e_t, s_t); l_t \in \{0, 1\}; t = 0, 1, \dots, N_O - 1, \quad (1)$$

where N_O is the number of CAD modeling steps. We use O_T to define the construction of the CAD model up until step T , i.e., the current state achieved by executing all (o_t, l_t) with $t \leq T$. Next, we explain how o_t is described by a 2D sketch s_t and extrusion e_t . The sketch s_t is organized as a "sketch-face-loop-curve" hierarchy. A sketch can contain one or more faces, where a face is a 2D region bounded by one or multiple loops. A loop is a closed 2D path consisting of one or more curves. A curve is either a line segment, an arc, or a circle. See Fig. 4 for an example. A sketch s_t is represented as a nested sequence:

$$s_t = \left[(c_t^0, \varepsilon_c), \varepsilon_l, \dots, \varepsilon_l, \dots, \varepsilon_l, \dots, \varepsilon_l, \varepsilon_f, \varepsilon_s \right], \quad (2)$$

where $\varepsilon_c, \varepsilon_l, \varepsilon_f, \varepsilon_s$ denote the tokens to mark the end of a curve, loop, face, and sketch, respectively. c_t^0 is a list of four 2D coordinates $[(\zeta_x, \zeta_y), \dots] \in \mathbb{R}^2$ to represent the outer circle in Fig. 4. To distinguish between the three types of curves, a line segment is described by 2 points, an arc by 3, and a circle by 4. The extrusion operation e_t transforms the sketch s_t into an extrusion cylinder o_t :

$$e_t = [d^+; d^-; \tau_x; \tau_y; \tau_z; \theta; \phi; \rho; \sigma; \varepsilon_e]. \quad (3)$$

Specifically, the 2D sketch is scaled with a factor of $\sigma \in \mathbb{R}$ and then transformed to the sketch plane with orientation $[\theta, \phi, \psi] \in \mathbb{R}^3$ and translation $[\tau_x, \tau_y, \tau_z] \in \mathbb{R}^3$. $[d^-, d^+]$ represents the extruded distances along (or opposite) the sketch plane normal. An illustration is shown in Fig. 4. Each extrusion cylinder o_t is combined with the previous state O_{t-1} using Boolean operation l_t , where l_t is 1 for the Union or 0 for Subtraction. In our implementation, we adopt the discrete tokenization in SkexGen [Xu et al. 2022] as the CAD DSLs to facilitate further autoregressive model learning. Additional details on the DSL tokenization and CAD modeling sequences can be found in Supp. A.

3.2 Pipeline Overview

Given an input 3D CAD model as point cloud $p_{\text{full}} \in \mathbb{R}^{N_p \times 3}$ consisting of N_p points, we learn to reconstruct an output CAD modeling sequence O encoded by the CAD DSL. To tackle the problem, we present an iterative prompt-and-select pipeline as illustrated in Fig. 3. For each iteration t , the method executes the following algorithmic steps.

Geometric Guidance Computation: We can analyze the previous state defined by CAD modeling sequence O_{t-1} and point cloud p_{full} to compute two forms of geometric guidance. First, we make use of the fact that extrusion cylinders have a planar bottom and

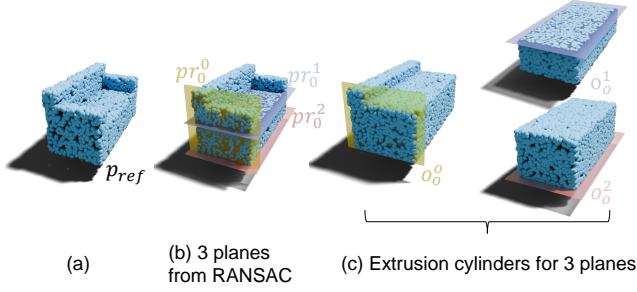


Fig. 5. An illustration of p_{ref} for the first step in Fig. 3, 3 detected planes from RANSAC, and their corresponding extrusion cylinders $o_0^i = (s_0^i, e_0^i)$. Only 3 detected planes are shown for simplicity.

top surface. We detect a set of candidate planes that are possible starting points for the next CAD modeling step (o_t, l_t) . These planes are encoded as planar prompts pr_t^i . Further, we compute a point cloud p_{ref} that encodes the difference between p_{full} and the previous state O_{t-1} as additional geometric guidance. We encode O_{t-1} by sampling it as point cloud $p_{prev} \in \mathbb{R}^{N_p \times 3}$.

Single-Step Reconstruction: The single-step reconstruction module at step t takes as inputs the planar prompts pr_t^i , the target point cloud p_{full} and the point cloud describing the previous state p_{prev} . We compute a possible CAD modeling step (o_t^i, l_t^i) for each sampled prompt pr_t^i (see the illustration in Fig. 5).

Single-Step Selection: The single-step selection module at step t takes all candidate CAD modeling steps (o_t^i, l_t^i) as input. We evaluate the fitness of each CAD modeling step and select the one with the highest fitness. For example, the CAD modeling step (o_0^1, l_0^1) is chosen in the step-0 of Fig. 3(c). Then, we concatenate the chosen CAD modeling step (o_t, l_t) to the previous state O_{t-1} and continue with the next iteration.

The method iteratively executes the above three modules until a stop criterion is achieved, e.g., the reconstruction error is small enough. The final output is denoted as O .

3.3 Common Modules

Point cloud encoder. We require a building block that can take an arbitrary point cloud and convert it into a set of tokens (features). We use the popular framework Point-MAE [Pang et al. 2022] to obtain point cloud features. We pre-train Point-MAE based on a point cloud reconstruction task following the official repo¹ with input point cloud p_{full} on the training dataset. Note that this pre-training is independent of the DSL sequence reconstruction. Once Point-MAE is trained, we only keep the Point-MAE encoder for point cloud features extraction. During training, we froze the first three layers and finetuned the last three layers so that the network could be adapted for our specific tasks. The point cloud encoder can encode an input point cloud p to a set of tokens (features) f . For example, in later sections, we use f_{full} , f_{prev} , and f_{ref} to denote the features computed for p_{full} , p_{prev} , and p_{ref} , respectively.

¹<https://github.com/Pang-Yatian/Point-MAE>

4 GEOMETRIC GUIDANCE COMPUTATION

The geometric guidance computation module at iteration (time step) t takes the point cloud of the complete input CAD model p_{full} as input. As additional input, we execute the token sequence describing the previous state O_{t-1} and sample the resulting CAD model with point cloud p_{prev} . As output we compute a set of candidate prompts pr_t^i .

Point Cloud Segmentation First, we would like to identify the distinct regions between p_{full} and p_{prev} . The distinct region of p_{full} compared to p_{prev} represents the geometry not yet covered by p_{prev} , while the distinct region of p_{prev} compared to p_{full} contains auxiliary points in the construction that will no longer be present in the final model. For example, given an observation in Fig. 6(b), p_{full} represents a sofa model, and p_{prev} represents its base. The distinct region of p_{full} corresponds to the armrest of the sofa. However, point clouds for the bottom face of the armrest are absent in p_{full} since it is sampled from the surface of the sofa, and the missing point cloud is complemented by the distinct region of p_{prev} . We train a segmentation network to predict binary masks \mathcal{M} on p_{full} and p_{prev} , labeling points with 1 if they belong to a distinct region. The segmentation mask \mathcal{M} is then applied to p_{full} and p_{prev} to get distinct point cloud regions p_{ref} . We use the notation $\mathcal{M}_{full}(p_{full})$ and $\mathcal{M}_{prev}(p_{prev})$ to denote an operation that returns the points with label 1 from the point cloud p_{full} and p_{prev} , respectively. The point cloud p_{ref} is simply the concatenation of $\mathcal{M}_{full}(p_{full})$ and $\mathcal{M}_{prev}(p_{prev})$.

Plane Detection We detect a set of candidate planes with an off-the-shelf RANSAC method and encode them as planar prompt pr_t^i . A planar prompt is encoded by randomly sampling 64 inlier points from a plane detected by RANSAC.

5 SINGLE-STEP RECONSTRUCTION

This section presents a module that takes the point cloud p_{ref} and a single prompt pr_t^i as input and outputs a candidate CAD modeling step (o_t^i, l_t^i) as depicted in Fig. 6(a). This module is executed for each prompt pr_t^i separately, but the point cloud p_{ref} is shared between all separate executions of the module.

We first discuss the network architecture. We use three decoders (Fig. 6) to predict three components of a CAD modeling step: sketch decoder (s -dec) for s_t , extrude decoder (e -dec) for e_t , and Boolean operation decoder (l -dec) for l_t . In addition, we use a simple module for prompt embedding. See Fig. 6 for an illustration of the architecture. We describe the individual components next.

Prompt embedding. Prompt embedding is computed by embedding the prompt point cloud pr_t^i using the point embedding part of the point cloud encoder. This embedding creates one token (feature vector) per point. We denote the output of this embedding as f_{pr}^i .

Sketch decoder and extrude decoder. Both sketch decoder s -dec and extrude decoder e -dec adopt the same transformer architecture for autoregressive sequence prediction, implemented as 6 stacked transformer decoder blocks shown in Fig. 6(c). Therefore, we describe them together. The input at each iteration of s -dec and e -dec are point cloud p_{ref} , prompt pr_t^i , and the current sequence of tokens

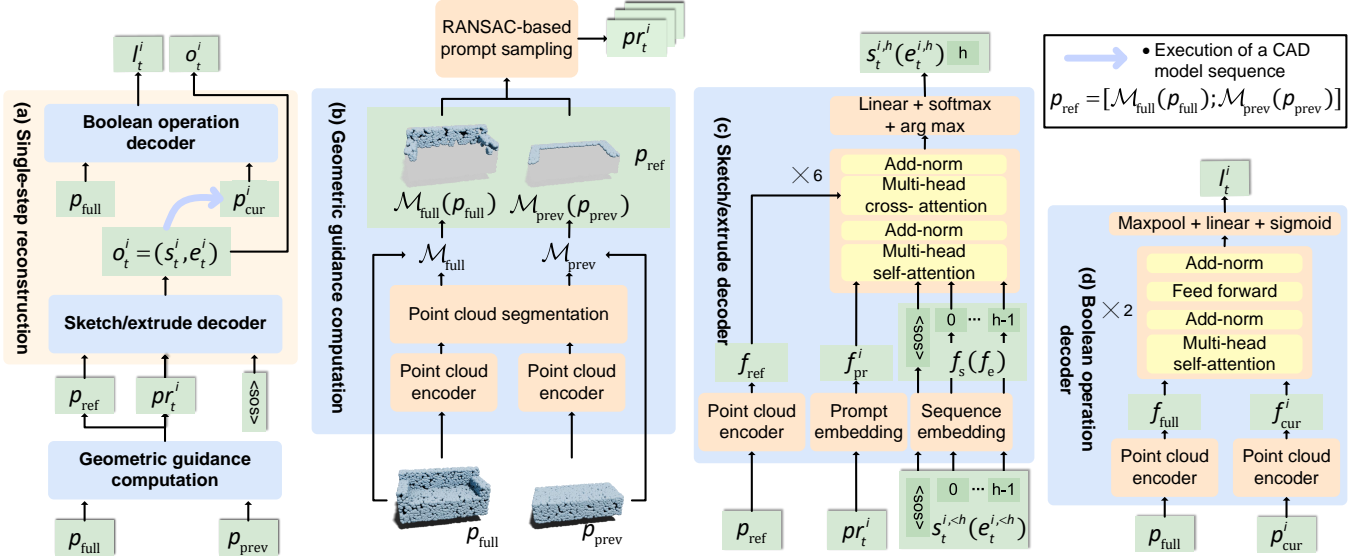


Fig. 6. Illustration of *Geometric Guidance Computation* and *Single-Step Reconstruction*. Geometric guidance computation takes the point cloud p_{full} and p_{prev} as input. It outputs the difference between p_{full} and p_{prev} as p_{ref} and a list of prompts pr_t^i detected from p_{ref} . The single-step reconstruction module consists of a sketch/extrude decoder and a Boolean operation decoder. The prompt pr_t^i , the point cloud p_{ref} , and a start token $\langle SOS \rangle$ are fed into the sketch-extrude decoder to autoregressively predict a sketch s_t^i and an extrude operation e_t^i defining the extrusion cylinder $o_t^i = (s_t^i, e_t^i)$. The Boolean operation decoder predicts l_t^i based on the input p_{full} and p_{cur}^i , where p_{cur}^i is obtained by executing o_t^i . At last, l_t^i and o_t^i are combined as the output of single-step reconstruction.

($s_t^{i,<h}$ or $e_t^{i,<h}$). Since both modules work in an auto-regressive manner, the modules themselves operate iteratively building the output sequences ($s_t^{i,<h}$ or $e_t^{i,<h}$) one step at a time. We use h to denote the iteration. We use $s_t^{i,<h}$ as shorthand to denote the sequence $s_t^{i,0}, s_t^{i,1}, \dots, s_t^{i,h-1}$. In the first iteration, $s_t^{i,0}$ or $e_t^{i,0}$ are initialized with the start token $\langle SOS \rangle$. First, all inputs are encoded: p_{ref} is encoded with the point cloud encoder to yield f_{ref} , pr_t^i is encoded to yield f_{pr}^i and $s_t^{i,<h}$ ($e_t^{i,<h}$) is encoded to yield the sequence embedding of the sketch(extrude).

The Queries of the self-attention and cross-attention layers in s -dec (e -dec) q_{s-dec} (q_{e-dec}) are the concatenation of f_{pr}^i and the sequence embedding of $s_t^{i,<h}$ ($e_t^{i,<h}$). The same tokens also serve as keys and values for the self-attention layers. For the multi-head cross-attention layers, point cloud features f_{ref} , serve as Keys and Values.

To output the next token, each token is assigned a softmax probability. An arg max operator is followed to get the token value as follows:

$$\begin{aligned} s_t^{i,h} &= \arg \max_j \left(s\text{-dec}(q_{s\text{-dec}}^{<h}, f_{ref})^j \right), s\text{-dec}(\cdot, \cdot) \in \mathbb{R}^{1 \times Q_s}, \\ e_t^{i,h} &= \arg \max_j \left(e\text{-dec}(q_{e\text{-dec}}^{<h}, f_{ref})^j \right), e\text{-dec}(\cdot, \cdot) \in \mathbb{R}^{1 \times Q_e}, \end{aligned} \quad (4)$$

j is the component index of the output probability, with a range of $[0, Q_s - 1]$ in $s\text{-dec}(\cdot, \cdot)$ and $[0, Q_e - 1]$ in $e\text{-dec}(\cdot, \cdot)$. Q is the number of different discrete tokens for a sketch or an extrusion operation as defined in SkexGen. We then execute the predicted s_t^i, e_t^i for a shape, from which we extract point clouds p_{cur}^i and compute features f_{cur}^i .

Boolean operation decoder. We implement l -dec as a transformer following a "Max-pooling + Linear + Sigmoid" layer, as depicted in Fig. 6(d). The l -dec takes f_{cur}^i and f_{full}^i as input, predicting a scalar in the range of $[0, 1]$ to represent l_t^i .

Training objective. We train s -dec and e -dec using teacher forcing [Kolen and Kremer 2001] and cross-entropy loss L_{CE} , and train l -dec with binary cross-entropy loss L_{BCE} . However, such an objective does not lead to a good performance. Experiments show the derived shape of the output sequence o_t largely differs from the supervision-executed shape in geometric structure and appearance. We believe this is caused by the huge domain gap between sequential and geometric representation [Ma et al. 2023], and we propose a geometric objective term to map the sequential output to the geometric representation space. Following Eq. 5, we construct a 3D bounding box of the executed shape of o_t , and calculate its intersection-over-union (IoU) with the bounding box of the supervision-executed shape,

$$L_{\text{bbox}} = -\ln \left[\text{IoU} \left(\text{bbox}(o_t^i), \text{bbox}(o_t^{\text{gt}}) \right) \right] \quad (5)$$

where o_t^{gt} is the supervision of o_t , indicating the ground-truth extrusion cylinder for the step t . The $\text{bbox}(\cdot)$ is a differentiable operator to construct a 3D bounding box from o_t^i or o_t^{gt} . The bounding box of an executed shape of a sketch-extrude sequence is illustrated in Fig. 4(c). The overall objective function is Eq. 6, where L_{bbox} is only enforced after ep_{thres} training epochs.

$$L_o = L_{CE} + L_{BCE} + \alpha L_{\text{bbox}}, \quad \alpha = \begin{cases} 1, & \text{if } \text{ep} > \text{ep}_{\text{thres}} \\ 0, & \text{otherwise} \end{cases} \quad (6)$$

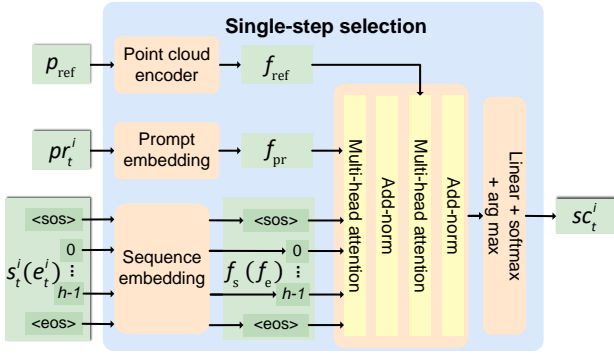


Fig. 7. The architecture of the single-step selection module. At step t , the single-step selection module takes the point cloud p_{ref} , a prompt pr_t^i , and a set of candidate CAD modeling steps $\{(o_t^i, l_t^i)\}$, and predicts a fitness score sc_t^i for each (o_t^i, l_t^i) in the set.

Implementation details. We leave implementation details of the differentiable bounding box construction $\text{bbox}(\cdot)$ in Supp. D.1, and training strategy in Supp. D.2.

6 SINGLE-STEP SELECTION

The single-step reconstruction module generates multiple candidate CAD modeling steps (o_t^i, l_t^i) . Here, we propose an architecture component that assigns probabilities to the different candidates. Though each choice (o_t^i, l_t^i) consists of a sequence of tokens with corresponding probabilities (cf. Eq. 4), the probabilities are conditioned on a specific prompt. Therefore, we cannot directly compute the overall probability of each candidate CAD modeling step.

To rate different CAD modeling steps, we present a single-step selection module for addressing this task. The module is trained to measure the geometric fitness of candidate CAD modeling steps, which therefore avoids the confusion due to pertaining to the GT step, while being more efficient than brute-force enumeration that executes all candidate commands and compares them in retrospect. We use the same mathematical notations as Sec. 5 for convenience and readability.

Network architecture. A visualization of the network architecture is shown in Fig. 7. The single-step selection module (denoted as $f\text{-dec}$) takes the point cloud p_{ref} , a single prompt pr_t^i , and a candidate CAD modeling step (o_t^i, l_t^i) as input and outputs a value $sc_t^i \in [0, 1]$ representing the fitness of (o_t^i, l_t^i) . The $f\text{-dec}$ is implemented in the same architecture as the sketch/extrude decoder in Fig. 6(c), except the output layer is modified from the "Linear + softmax + arg max" to the "Linear + sigmoid". For the input, the point cloud p_{ref} , the prompt pr_t^i , and (o_t^i, l_t^i) are encoded to yield f_{pr} , f_{pr}^i and the sequence embedding. The Query of $f\text{-dec}$ ($q_{f\text{-dec}}$) is the concatenation of f_{pr}^i and the sequence embedding of (o_t^i, l_t^i) . f_{ref} serves as Key and Value. The output is as follows:

$$sc_t^i = f\text{-dec}(q_{f\text{-dec}}, f_{\text{ref}}), f\text{-dec}(\cdot, \cdot) \in \mathbb{R}^{1 \times 1}. \quad (7)$$

Training objective. The single-step selection module essentially performs a regression task and we choose the commonly used L1 loss as the objective function for step t , $L_t^{\text{sc}} = |sc_t^i - sc_t^{\text{gt}}|$. sc_t^{gt} denotes the supervision of the fitness score for (o_t^i, l_t^i) as defined in Eq. 8. Since sc_t^{gt} cannot be directly obtained from the existing dataset [Wu et al. 2021], we calculate sc_t^{gt} by comparing the geometric similarity between the executed shapes of o_t^i and ground-truth o_t^{gt} . The intuition is that (o_t^i, l_t^i) cannot be concluded as unsuitable even if it is dissimilar to $(o_t^{\text{gt}}, l_t^{\text{gt}})$. Instead, it is more reliable to compare the similarity between their unique executions. We formulate sc_t^{gt} as the bounding box intersection-over-union (IoU) between the executed shape of o_t^i and o_t^{gt} , multiplied by the binary value of the l_t^i and l_t^{gt} consistency, where the $\text{bbox}(\cdot)$ is the same as that in Eq. 5.

$$sc_t^{\text{gt}} = \begin{cases} \text{IoU}(\text{bbox}(o_t^i), \text{bbox}(o_t^{\text{gt}})), & \text{if } l_t^i = l_t^{\text{gt}}, \\ 0, & \text{otherwise.} \end{cases} \quad (8)$$

We use the bounding box IoU to approximate the geometric similarity for two reasons. First, calculating the bounding box IoU is more straightforward compared to calculating the fine-grained IoU between shapes. Second, the bounding box can accurately reflect the principal parameters of the sketch-extrude sequence constructing the shape (cf. Extrude value, Sketch plane orientation, etc. in Fig. 4).

7 EXPERIMENTS AND ANALYSIS

In this section, we provide a quantitative and qualitative evaluation, an ablation study, and a robustness test of our method.

7.1 Experimental Setup

Datasets. We use the DeepCAD [Wu et al. 2021] dataset for training. Following the dataset split of DeepCAD, we train the networks on the DeepCAD train set and report results on the DeepCAD test set. We also report the cross-dataset generalization based on the Fusion360 [Willis et al. 2021] dataset. For all input CAD models, we randomly sample 8192 points on the surface as input point clouds.

Evaluation metrics. We evaluate the geometric quality following [Guo et al. 2022a] and sequence fidelity using NLL used to evaluate similar auto-regressive generative models. Geometric metrics are calculated between the input CAD models and the execution of predicted CAD modeling sequence O with the following terms:

- Chamfer distance (CD) and Hausdorff distance (HD) of 16382 randomly sampled points on the geometry surface of two shapes for geometry distance.
- Edge chamfer distance (ECD) to compute the distance between edge points of two CAD models to reflect the structure similarity.
- Normal consistency (NC) to measure the cosine similarity between corresponding normals as the smoothness of predicted shapes.
- Invalidity Ratio (IR) to measure the ratio of CAD modeling sequences that cannot be executed.

We use the point cloud of the ground-truth CAD model and the point cloud of output CAD modeling sequence execution to compute geometric metrics. For a scale-invariance comparison, we normalize the

ground-truth CAD model and reconstruction into a unit bounding box keeping the aspect ratio. To determine whether a reconstruction is invalid, we retain the output of each step (O_0, O_1, \dots). If none of them leads to a successful execution, we consider it to be invalid. We use the Negative log-likelihood (NLL) of the auto-regressive model to evaluate the sequence fidelity produced by the single-step reconstruction module. Specifically, given the point cloud of the input CAD model and that of the ground-truth previous state, we predict the logits of the next CAD modeling step and calculate the NLL. We evaluate the quality of sketch and extruding, separately with ske_NLL and ext_NLL .

Baselines. We compare with four SoTA methods [Li et al. 2023a; Uy et al. 2022; Wu et al. 2021; Xu et al. 2023, 2021] focusing on the reverse engineering of CAD modeling sequences. We compare with these methods by running the available codes and pre-trained weights with the same test splits for a fair comparison. Point2Cyl [Uy et al. 2022] applies instance segmentation on point cloud of the input CAD model. Each instance is treated as a potential extrusion cylinder and another segmentation is applied to locate the cross-section (base) and side surface (barrel). Afterward, Point2Cyl fit for an extrusion operation and a sketch utilizing base and barrel. SECAD-Net [Li et al. 2023a] requires both voxel and point cloud as inputs. We apply mesh-voxelization [Stutz 2017; Stutz and Geiger 2018] to convert the mesh of a CAD model into a $64 \times 64 \times 64$ voxel. It outputs a fixed number of CAD modeling steps and we follow its official implementation to output 4 CAD modeling steps. Since SECAD-Net employs unsupervised learning, it can overfit to each test data to get the best reconstruction result. HNC-CAD is initially designed for CAD modeling sequence generation. We train HNC-CAD by feeding it with the point cloud features of the input CAD model, without changing any output to adapt it to perform CAD modeling sequence reconstruction. We do not compare with [Lambourne et al. 2022] and the concurrent work [Khan et al. 2024], because they do not release the source code.

Implementation details. For geometric guidance computation (Sec. 4), we train the point cloud segmentation network for 80 epochs with a batch size of 256. An AdamW optimizer with an initial learning rate of $1e-3$ is employed for optimization and the learning rate is scheduled by a cosine annealing scheduler until the minimal learning rate of $1e-6$. We train the single-step reconstruction (Sec. 5) based on the objective function of Eq. 6. The network is trained for 200 epochs with a batch size of 224 on 1 A100-80G GPU, using the AdamW optimizer with a learning rate of $1e-3$. The learning rate drops to $9e-5$ after the initial 90 epochs and gradually decreases to the minimal learning rate of $5e-6$ based on the cosine annealing scheduler. We empirically set the ep_{thres} in Eq. 6 as 30. The single-step selection (sec. 6) is trained for 100 epochs with a batch size of 224 on 1 A100-80G GPU, using the same optimizer and learning rate scheduler as the single-step reconstruction.

7.2 Comparison with the State of the Art

Main comparison. In Tab. 1, we quantitatively show the performance of all the competing methods. Directly predicting a CAD

Table 1. Quantitative comparisons of geometric metrics of different methods on DeepCAD and Fusion360. CD, HD, and ECD are scaled by 10^2 . In DeepCAD, our method improves over SECAD-Net by 10% on geometric error (CD, HD) and 16% on structural error (ECD). In Fusion360, our method also shows better geometric quality than SECAD-Net, but has a lower invalid reconstruction ratio (IR).

Dataset	Method	CD ↓	HD ↓	ECD ↓	NC ↑	IR (%) ↓
DeepCAD	DeepCAD	4.25	39.25	19.33	0.49	7.14
	HNC-CAD	1.09	20.23	5.94	0.75	0.32
	Point2cyl	1.00	20.93	20.45	0.73	0.0
	SECAD-Net	0.42	9.96	5.54	0.73	0.38
	Ours (PS-CAD)	0.21	8.66	4.65	0.89	0.43
Fusion360	HNC-CAD	1.38	20.61	9.24	0.52	0.33
	SECAD-Net	0.69	12.76	5.15	0.64	3.82
	Ours (PS-CAD)	0.57	12.0	5.02	0.67	1.51

Table 2. Quantitative comparison of the negative log-likelihood (NLL) of sequentially-based reconstruction methods.

Method	ext_NLL ↓	ske_NLL ↓
HNC-CAD	38.66	103.33
Ours (PS-CAD)	1.61	25.51

modeling sequence as the CAD DSL sequence, e.g., DeepCAD [Wu et al. 2021] and HNC-CAD [Xu et al. 2023] for this task results in poor performance because aligning point clouds with a CAD DSL is difficult. Our proposed method PS-CAD significantly improves upon all SOTA methods on all geometric metrics on DeepCAD. We can reduce the geometry errors (CD and HD) by at least 10%, and the structural error (ECD metric) by about 15%. Moreover, the proposed method can attain the best normal quality. The generalization comparison on Fusion360 yields better results than HNC-CAD and SECAD-Net. We reduce the geometry errors by at least 5% and the structural error by about 2.5%.

We show a comparison of the NLL in Tab. 2. We can only compare to the similar auto-regressive model HNC-CAD and we note a huge improvement in the metrics. This suggests that geometric guidance can greatly improve the accuracy of predicting CAD DSL sequences.

Qualitative comparison. In Fig. 8 and Fig 9, we qualitatively show the performance on DeepCAD and Fusion360 of the competing methods. Note that our point cloud visualization shows the overall structure well, but seeing some of the detailed structures in the input point cloud would require inspecting the point cloud in an interactive editor from multiple views (See Appendix Fig. 17). DeepCAD and HNC-CAD output a CAD DSL sequence. They can correctly reconstruct the coarse appearance of the input CAD models, but the structure as well as the details are often wrong. (see column DeepCAD, HNC-CAD in Fig. 8, column HNC-CAD in Fig. 9).

Point2Cyl and SECAD-Net reconstruct sketches with implicit representations and generally perform better than DeepCAD and HNC-CAD. Still, Point2Cyl and SECAD-Net also have problems with the details as well as the structure. Point2Cyl often predicts the main

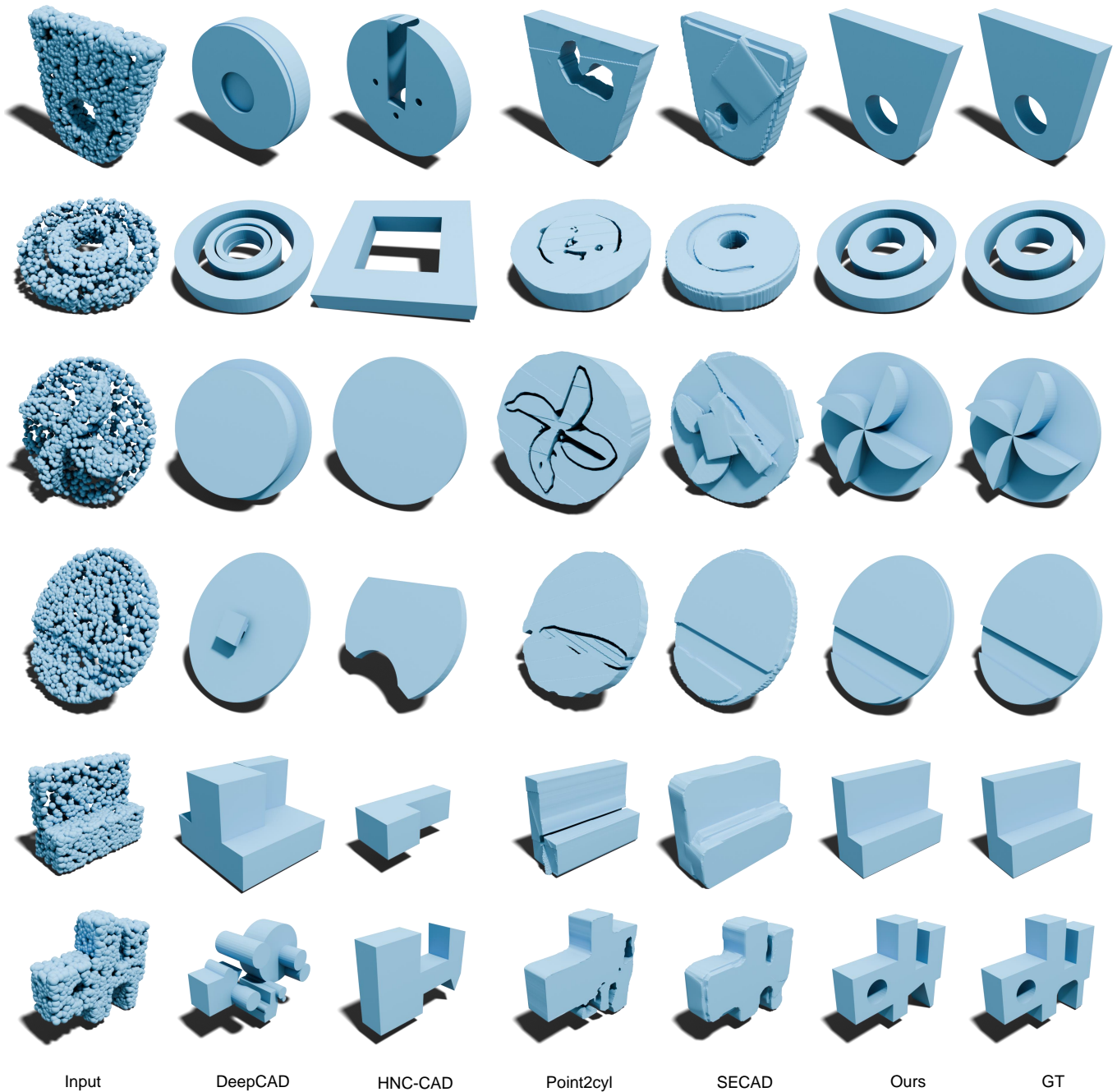


Fig. 8. Qualitative comparison of different methods on DeepCAD. Please zoom in to see the deviations from ground truth.

shape correctly, but it adds incorrect and overly complicated details (all rows in Fig. 8). SECAD-Net sometimes does not preserve the basic structures, e.g. crevices in the input (see row 2,3,6 in Fig. 8 and rows in Fig. 9) or invents erroneous details, e.g., a square extrusion cylinder in row 1 in Fig. 8. By contrast, our method reproduces the structure and the details of the input better. Our method is

also capable of reconstructing detailed geometry of inputs from a cross-domain dataset Fusion360, e.g., different kinds of holes in Fig. 9.

Table 3. Ablation study of the single-step reconstruction and the single-step selection module. For single-step reconstruction, we measure the effect of the different inputs when reconstructing one CAD modeling step. p_{full} : point cloud of the input CAD model; $[p_{full}; p_{prev}]$: point cloud of the input CAD model is concatenated with point cloud of previous state execution; p_{ref} : the distinct regions between p_{full} and p_{prev} . pr : the geometric prompt. We also evaluate the proposed bounding box loss L_{bbox} in Eq. 5. For the single-step selection module, we compare the performance of different selection strategies. "geo": the greedy selection based on the geometric criteria implemented as chamfer distance; "heur": selecting the candidate extrusion cylinder with the largest volume; "rand": random selection; "ours": using the single-step selection module.

Single-step reconstruction					Single-step selection				Metrics			
p_{full}	$[p_{full}; p_{prev}]$	p_{ref}	pr	L_{bbox}	geo	heur	rand	ours	CD	ext_NLL	ske_NLL	IR (%)
✓					✓				1.21	5.77	132.85	7.53
	✓				✓				0.67	2.24	91.03	6.85
		✓			✓				0.37	1.68	33.45	6.99
		✓	✓		✓				0.61	1.98	47.84	1.37
		✓	✓	✓	✓				0.28	1.59	30.10	0.69
		✓	✓	✓		✓			0.95	2.49	100.08	1.37
		✓	✓	✓			✓		1.48	7.95	213.27	1.51
		✓	✓	✓				✓	0.19	1.49	19.63	0.41

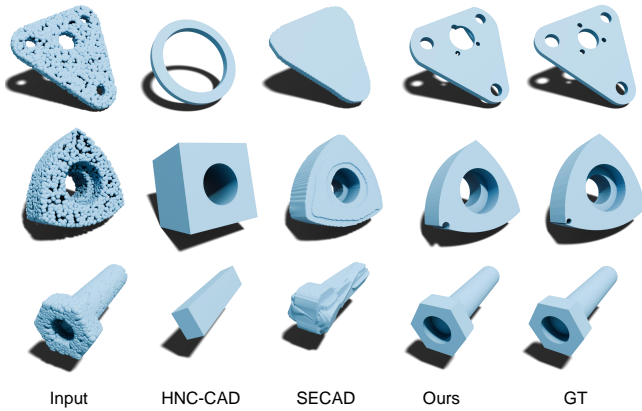


Fig. 9. Qualitative comparison of different methods on Fusion-360 to evaluate generalization capabilities. None of the methods were trained on Fusion-360.

7.3 Ablation Studies

In Tab. 3, we first show a set of ablations on the designs of the single-step reconstruction. We randomly select 730 input models for the ablation studies, which accounts for approximately 10% of the total test dataset. Note that we evaluate the designs of the single-step reconstruction with the selection strategy "geo". This is because the single-step selection is based on the output of the single-step reconstruction. When the output quality varies due to the ablation setting, the rating result of the single-step selection introduces extraneous factors that affect the ablation.

The effect of p_{ref} . The first three rows of Tab. 3 ablate the input fed to single-step reconstruction. Only given p_{full} leads to poor performance in geometric quality and sequence fidelity. It can only reconstruct the main structure and loses many details. Sometimes an invalid reconstruction is produced (see Fig. 10 p_{full}). With the help of p_{prev} , there is a noticeable reduction in the extrude NLL

(ext_NLL). By explicitly identifying the distinct regions of p_{full} and p_{prev} with a binary mask \mathcal{M} , the network can distinguish which part has already been completed for reconstruction, and which part still needs further work. Using the mask gives a cleaner geometric context and improves the sequence fidelity, reflected in further reductions in sketch NLL and extrude NLL.

The effect of pr . By providing a prompt to the single-step reconstruction, albeit with a decrease in geometric reconstruction quality, it improves the reconstruction invalid rate. This suggests that the prompt improves the tolerance to input CAD models with different shapes. We believe the source of this ability is that the prompt can provide guidance for local geometric context encoding. This local geometric context, compared with p_{ref} , can support the reconstruction of one valid CAD modeling step with better efficiency.

Single-step selection. Afterward, we fix the setting of single-step reconstruction and validate the single-step selection by comparing it with different selection strategies. Among the other selection strategies, "geo" is based on the geometric quality of the candidate CAD modeling step. Take the step- t for example, we make temporary step- t O_t^i by combining the candidate CAD modeling step (o_t^i, l_t^i) with the state- $t-1$ output O_{t-1} . The execution of O_t^i as point cloud is compared with point cloud p_{full} of the input CAD model to calculate the chamfer distance. "geo" selects the O_t^{i*} with the lowest chamfer distance as the step- t output. "heur" is to select the extrusion cylinder o_t^{i*} with the largest volume. It follows a design convention that a CAD model is usually created by first constructing the main structure and then designing the details. "rand" is to randomly select a candidate CAD modeling step. The results show that the heuristic and geometric-based selection do not work as well for all inputs because they do not consider the structure of the input CAD model. For example in Fig. 11 row 3, the input is a combination of two extrusion cylinders. However, the side surface is sampled as a prompt and leads to a candidate CAD modeling step with a "T" shaped extrusion cylinder. This "T-shape" extrusion cylinder has the lowest chamfer distance with the input and has the largest volume

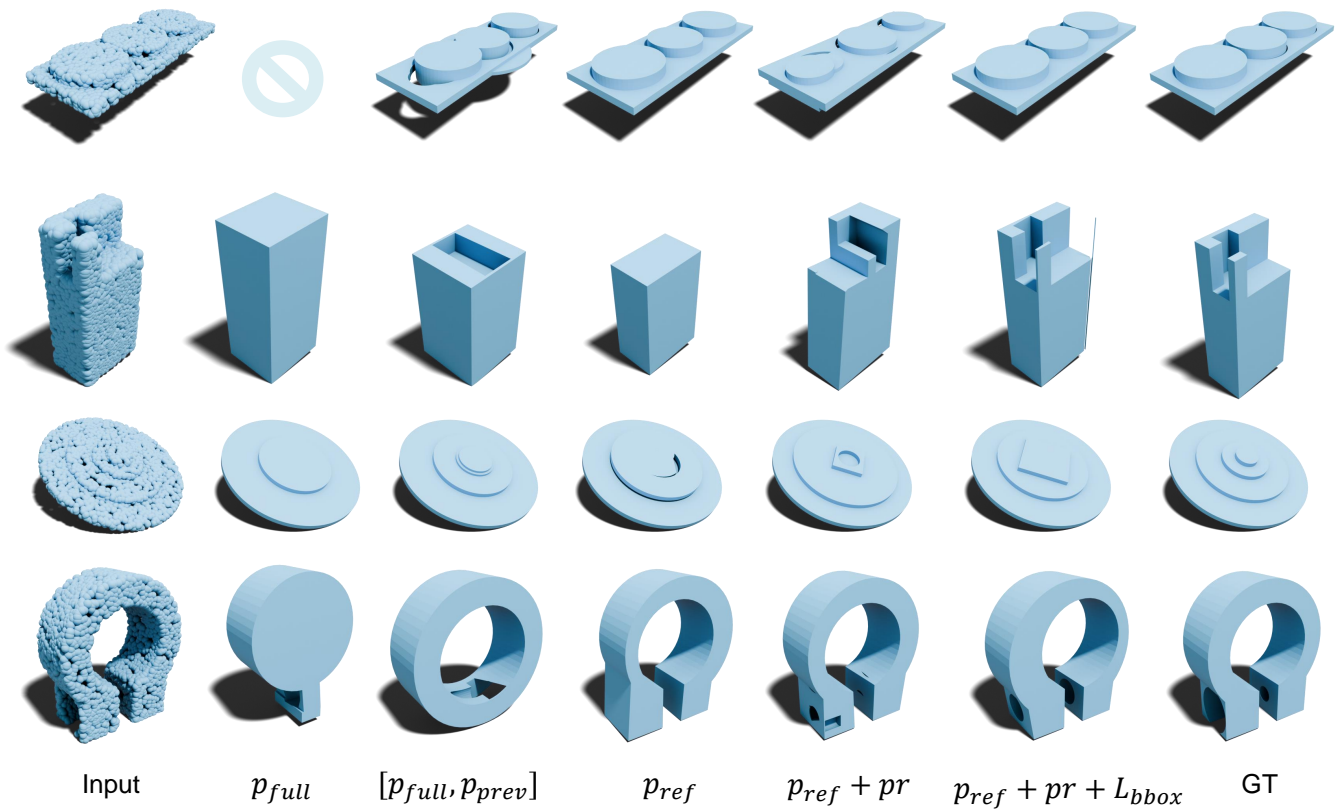


Fig. 10. Ablating different designs in single-step reconstruction. See the text for details about p_{full} , $[p_{full}; p_{prev}]$, p_{ref} , p_r , L_{bbox} .

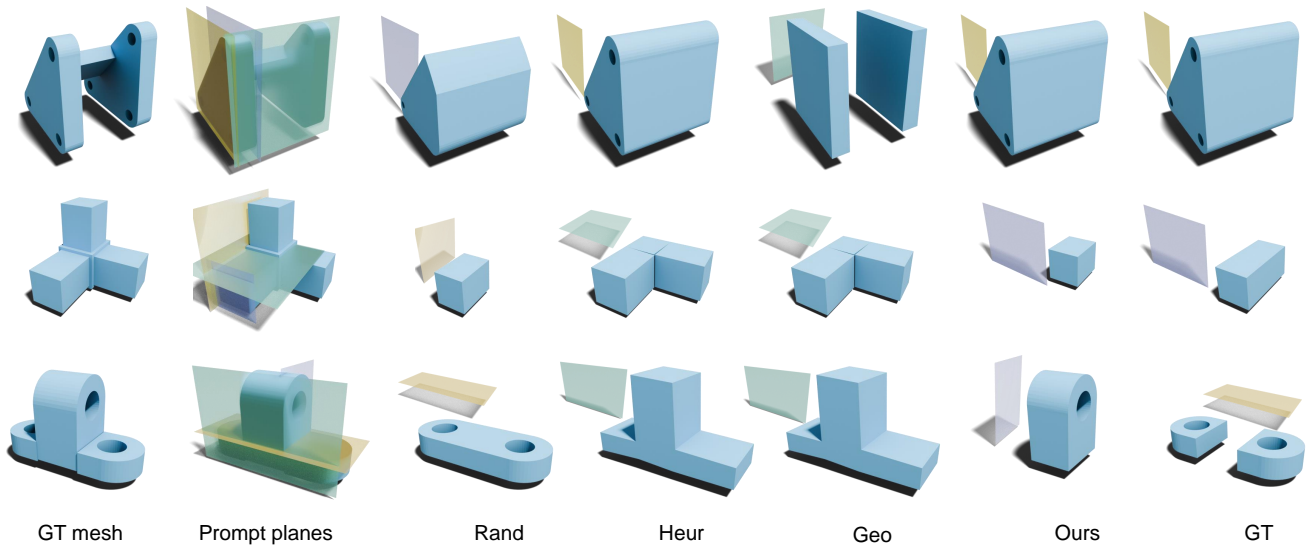


Fig. 11. Comparisons of different prompt selection methods. See the paper text for an explanation of the different selection methods.

among all the candidates. In Fig. 11 row 1, the heuristic-based selection works well, but the geometric-based selection performs badly and creates two boxes using the green prompt. The reason is that the chamfer distance of the CAD modeling step stemming from the green prompt is slightly better. The geometric-based selection then chooses the wrong candidate. By contrast, the single-step selection performs well in both cases, while it may select a different candidate from the ground-truth, the selected candidate can still correctly reflect the input structure.

7.4 Robustness test

In this section, we test the robustness of the single-step reconstruction module with respect to the prompt. We specifically test the effect of prompt sampling under different conditions, including the number of points of a sampled prompt, the source (sampled from either p_{full} or p_{ref}), and the quality of the prompt-sampling plane. Finally, we visualize some reconstruction results when our method is fed with noisy point clouds of the input CAD model.

Prompt. In Tab. 4-Sampling location, we detect planes from point clouds of different sources (p_{full} or p_{ref}) and sample prompts from these planes. Results show that if the planes are sampled from the point cloud p_{full} of the input CAD model in step-wise reconstruction, the performance decreases in all metrics. The extrude and sketch NLL deteriorate more than 100% ($0.19 \rightarrow 0.48$) and 400% ($1.49 \rightarrow 3.18$). If a prompt is always from p_{full} , it lacks the ability to adapt to the dynamically changing geometric context in the iterative reconstruction.

In Tab. 4-Sampling number, we verify the effect of the number of points within a prompt. Given planes detected from the point cloud p_{ref} , the prompts with fewer points lead to a higher reconstruction invalid ratio (prompt points $64 \rightarrow 16$, IR $0.41 \rightarrow 0.83$).

Since the prompt relies on RANSAC-detected planes, they do not always match the surface of extrusion cylinders to a high degree. In Tab. 5-Perturbations on planes, we sample prompts from planes with different corruptions, including plane deficiency or (and) Gaussian noise. Results show that our method is robust to the Gaussian noise added on prompts. When a prompt is sampled from a plane with deficiency, it cannot capture the sketch information and produces weaker reconstructions (ske_NLL from 19.51 to 33.99). This also leads to a higher invalid reconstruction ratio (IR) and chamfer distance (CD).

It is also critical to validate the effect of the RANSAC hyperparameters on prompt sampling. We test two of the hyperparameters in Tab. 5-Hyperparameters of RANSAC, namely t and d . t is the threshold value to determine when a point is detected to fit a plane. If t increases, the detected plane deviates from the real sketch plane and produces worse sketches (ske_NLL from 19.51 to 81.64, when t from $1e-3$ to $1e-2$). Due to the association of extrusion and the sketch plane, the extrude quality also decreases (ext_NLL $1.49 \rightarrow 1.95$). These factors result in higher IR and CD. d is the number of inlier points required to assert that a plane is fitted. If d is provided with a larger number ($64 \rightarrow 128 \rightarrow 256$), some sketches located on a tinier plane would be omitted and this results in a higher IR ($0.27 \rightarrow 0.41 \rightarrow 2.30$).

Table 4. Effect of prompts sampled under different settings. In Sampling location, p_{full} denotes prompts sampled from the point cloud of the input CAD model to reconstruct an arbitrary CAD modeling step. p_{ref} denotes prompts from point cloud p_{ref} . In Sampling number, prompts with different numbers of points are evaluated (16, 32, and 64 respectively).

Sampling location		Sampling number			Metrics			
p_{full}	p_{ref}	16	32	64	CD	ext_NLL	ske_NLL	IR
√				√	0.48	3.18	107.04	1.78
	√			√	0.19	1.49	19.63	0.41
	√	√			0.19	1.53	20.46	0.83
	√		√		0.20	1.51	20.53	0.54

Table 5. Effect of prompts sampled from low-quality planar surfaces. In Perturbations on planes, Gaussian is to add Gaussian noise on the detected planes; deficiency 50% means randomly covering half of the detected plane. In Hyperparameters of RANSAC, t is the threshold value to determine when a point is detected to fit for a plane, and d is the number of inlier points required to assert that a plane is fitted.

Perturbations on planes		Hyperparameters of RANSAC		Metrics			
Gaussian	deficiency 50%	t	d	CD	ext_NLL	ske_NLL	IR
		$1e-3$	128	0.19	1.49	19.51	0.41
√		$1e-3$	128	0.19	1.53	20.33	0.54
	√	$1e-3$	128	0.34	1.69	33.99	1.65
√	√	$1e-3$	128	0.35	1.70	34.10	1.78
		$1e-3$	64	0.23	1.62	18.65	0.27
		$1e-3$	256	0.23	1.65	21.14	2.30
		$3e-3$	128	0.25	1.60	20.62	0.27
		$5e-3$	128	0.37	1.83	46.70	2.33
		$1e-2$	128	0.39	1.95	81.63	1.92

Table 6. Evaluation of different numbers of input points and point cloud encoder layers.

Point cloud config	E layer	CD ↓	ECD ↓	IR ↓
$N \in \mathbb{R}^{4096 \times 3}$	6	0.17	3.80	0.97
$N \in \mathbb{R}^{8192 \times 3}$	6	0.19	3.87	0.41
$N \in \mathbb{R}^{12288 \times 3}$	6	0.17	3.89	0.28
$N \in \mathbb{R}^{8192 \times 3}$	12	0.16	3.53	0.28

Point cloud corruptions and point cloud encoder. We validate the robustness of the method to different point cloud corruptions, like noises, sparsity, and partial point masking, in Fig. 12. We observe that the basic structure of a shape can be reconstructed, however, the local details are not consistent with the input CAD model due to noise or incomplete point clouds. We test the robustness of the method to different numbers of points in the input point clouds in Tab. 6. Results indicate sparse point clouds lead to worse results on geometric metrics. This is because point clouds with fewer points are not able to represent small-scale geometry making the CAD reconstruction with fine-level details difficult.

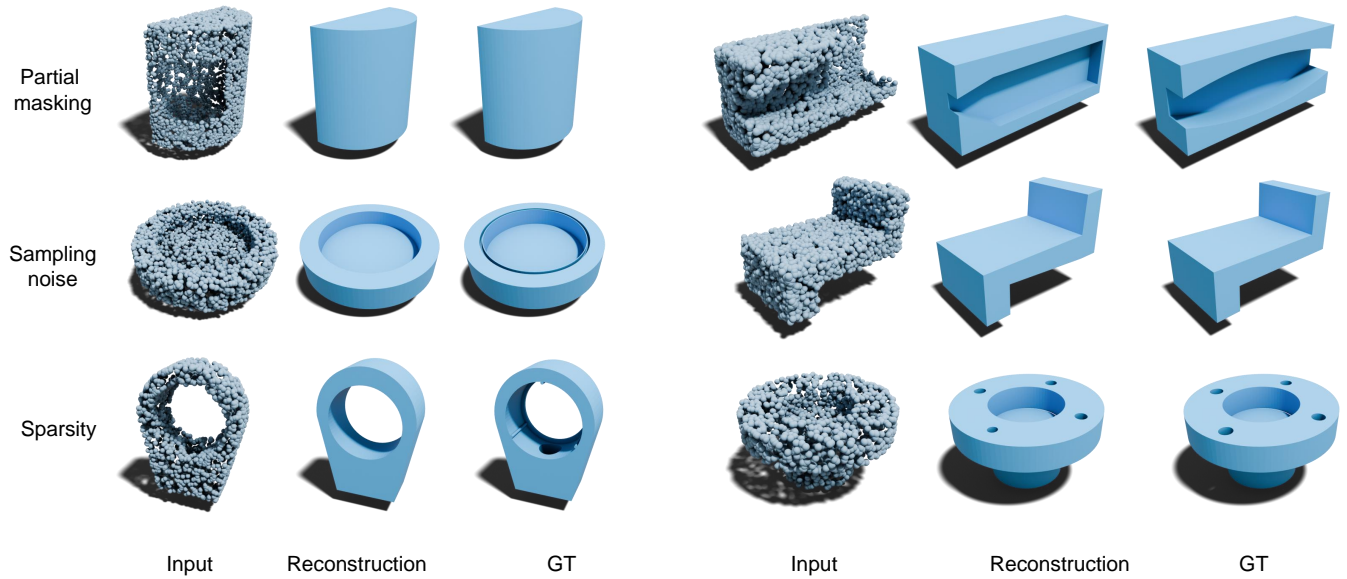


Fig. 12. Robustness validations for different cases, including partial point masking, adding noises, and increasing point cloud sparsity.

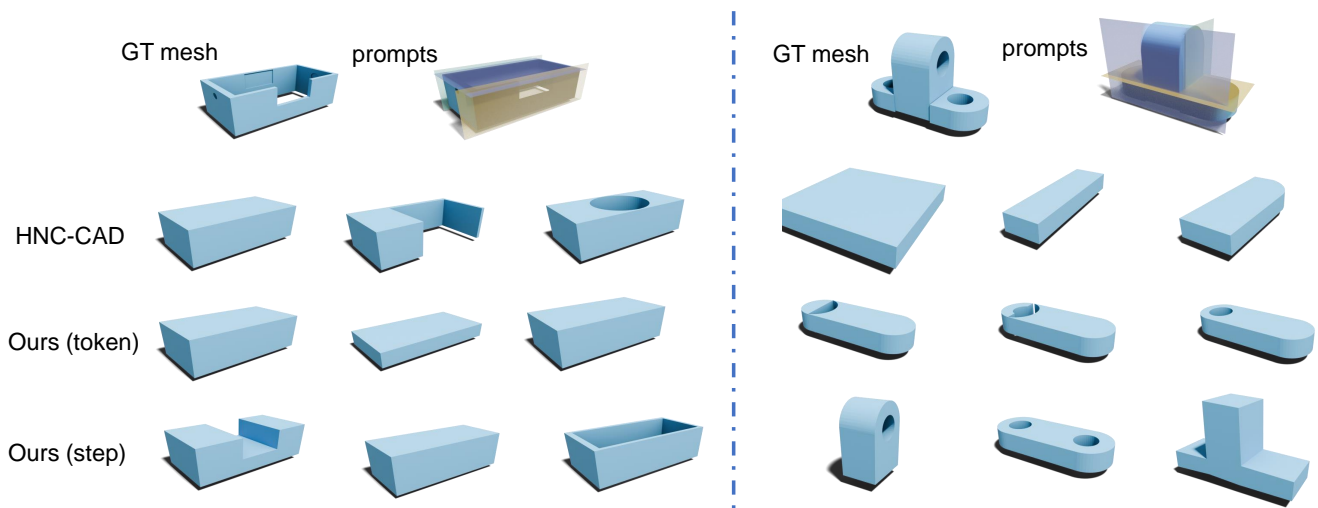


Fig. 13. Comparisons of two token-based sampling methods and ours on the sampling variations.

We also show the impact of different numbers of Transformer layers in the point cloud encoder. More Transformer layers can increase the representation capacity of the network, thus improving the metrics.

7.5 Discussions

Prompt sampling vs. Token sampling. In Fig. 13, we show the capability of prompt sampling over the token sampling of the autoregressive model. In HNC-CAD, the sampling results lead to diverse CAD modeling steps, but few of them convey the structure of the input model. In Ours (token), we turn to use token sampling to

produce candidate CAD modeling steps and the results are almost the same. With the help of prompt shown in different colors, Ours (step) can produce multiple reasonable candidates.

Relationship with cross-section-based methods. In geometric guidance computation, we sample planar prompts on RANSAC-detected planes. These planes are potential cross-sections which an extrusion cylinder can start from. As shown in Fig. 13, by utilizing prompts, our approach can reconstruct the extrusion cylinder highly correlated with the cross-section. From this perspective, our approach is similar to the cross-section-based method Point2Cyl. Different from Point2Cyl which uses a closed-form formulation to

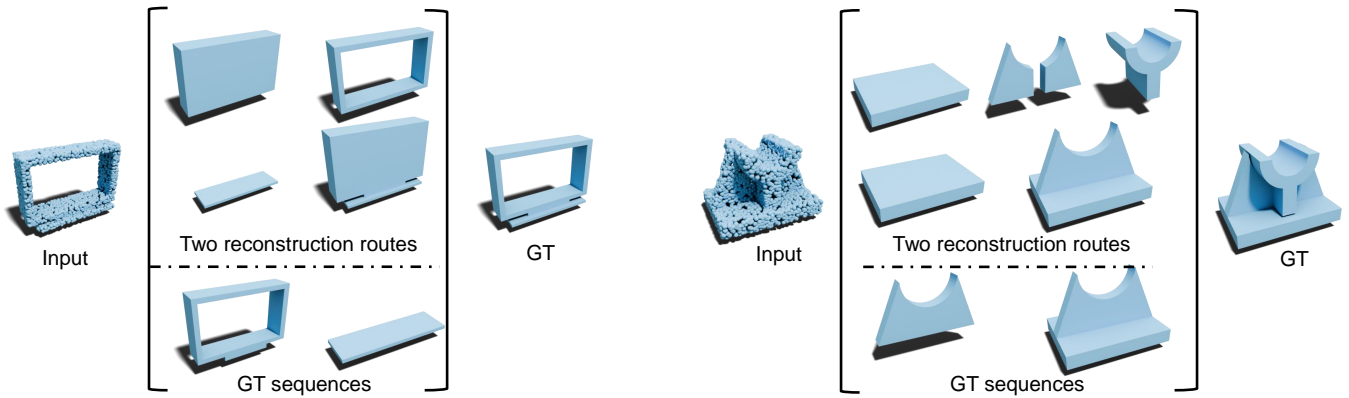


Fig. 14. Multiple feasible CAD sequences for a point cloud can be provided to reconstruct an input point cloud.

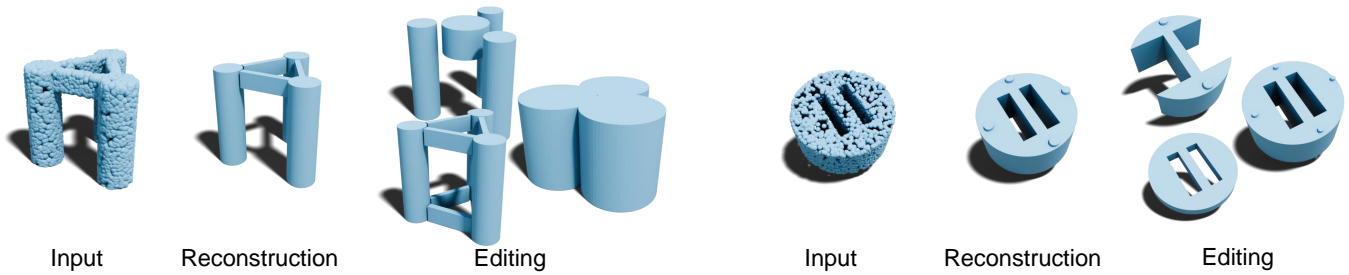


Fig. 15. Editing results for reconstructed CAD models.

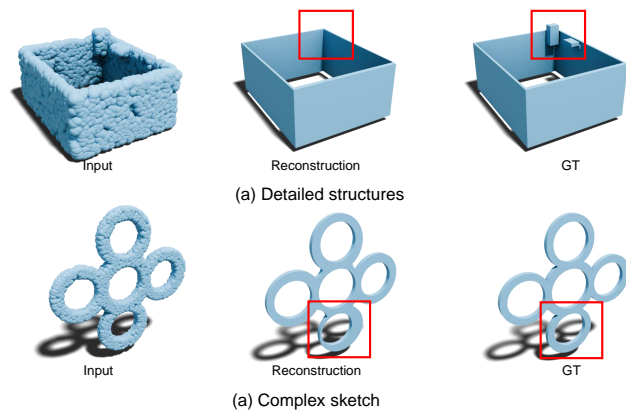


Fig. 16. Failure cases. The method has difficulty in recovering (a) details that are very small compared to the overall input shape and (b) complex sketches.

calculate extrusion parameters, we use the network to predict the extrusion operation. The network is more robust to the input and produces powerful geometric descriptors for reconstruction.

Failure cases. In Fig. 16, we demonstrate two typical failure cases. In the first case, the input shape contains an extrusion with a larger

size and two small blocks. The method fails to recover the two small blocks as they contain very few points. In the second case, the input shape is extruded from a complex sketch and the method predicts an invalid sketch that is too different from the input.

7.6 Applications

Interactive reconstruction. Our method can produce different reconstruction sequences for the same input. This advantage can be attributed to the promptable reconstruction, which facilitates multiple legitimate candidate reconstructions in each stage. In addition to always selecting the best candidate in the single-step selection, it is also possible to sample according to probabilities. Illustrations are shown in Fig. 14. This sampling can still lead to correct reconstructions.

Moreover, we can explore potential variations of a reconstructed CAD shape by editing parameters within the reconstructed CAD modeling sequence (e.g., see Figure. 15).

8 CONCLUSION AND FUTURE WORK

We present a prompt-and-select framework for sequential CAD modeling from point clouds. The method leverages local geometric information to guide the CAD reconstruction process of an autoregressive model. We provide plane-based prompts for better candidate sketch-extrusion sequence prediction. Extensive experiments

validate the method is effective and can outperform SoTA methods in geometry accuracy (CD, HD, and ECD metrics), valid ratios, and geometry regularity (NC). We also showcase that the method can be applied to reverse engineering and further geometry editing.

There are some limitations to our work. First, we did not consider the regularity constraints between different sketch-extrusions, e.g., co-axes, alignment, and orthogonal relations between different surfaces. Second, the method mainly focuses on the CAD modeling of sketch-extrusion-based shapes and does not deal with operations like sweeping and revolving surfaces. However, it should be possible to extend it to different kinds of CAD commands when corresponding datasets are available for training. Third, fine-grained geometry details usually pose challenges to both our method and previous work. These details are usually under-represented in input point clouds and optimization losses compared to larger geometry primitives.

REFERENCES

- Suzanne F. Buchele and Richard H. Crawford. 2004. Three-dimensional halfspace constructive solid geometry tree construction from implicit boundary representations. *Comput. Aided Des.* 36, 11 (2004), 1063–1073. <https://doi.org/10.1016/j.cad.2004.01.006>
- Boyang Deng, Kyle Genova, Soroosh Yazdani, Sofien Bouaziz, Geoffrey E. Hinton, and Andrea Tagliasacchi. 2020. CvxNet: Learnable Convex Decomposition. In *2020 IEEE/CVF Conference on Computer Vision and Pattern Recognition, CVPR 2020, Seattle, WA, USA, June 13–19, 2020*. Computer Vision Foundation / IEEE, 31–41. <https://doi.org/10.1109/CVPR42600.2020.00011>
- Tao Du, Jeevana Priya Inala, Yewen Pu, Andrew Spielberg, Adriana Schulz, Daniela Rus, Armando Solar-Lezama, and Wojciech Matusik. 2018. InverseCSG: automatic conversion of 3D models to CSG trees. *ACM Trans. Graph.* 37, 6 (2018), 213. <https://doi.org/10.1145/3272127.3275006>
- Kevin Ellis, Maxwell I. Nye, Yewen Pu, Felix Sosa, Josh Tenenbaum, and Armando Solar-Lezama. 2019. Write, Execute, Assess: Program Synthesis with a REPL. In *Advances in Neural Information Processing Systems 32: Annual Conference on Neural Information Processing Systems 2019, NeurIPS 2019, December 8–14, 2019, Vancouver, BC, Canada*, Hanna M. Wallach, Hugo Larochelle, Alina Beygelzimer, Florence d’Alché-Buc, Emily B. Fox, and Roman Garnett (Eds.). 9165–9174. <https://proceedings.neurips.cc/paper/2019/hash/50d2d2262762648589b1943078712aa6-Abstract.html>
- Pierre-Alain Fayolle and Alexander A. Pasko. 2016. An evolutionary approach to the extraction of object construction trees from 3D point clouds. *Comput. Aided Des.* 74 (2016), 1–17. <https://doi.org/10.1016/j.cad.2016.01.001>
- Noa Fish, Melinos Averkiou, Oliver van Kaick, Olga Sorkine-Hornung, Daniel Cohen-Or, and Niloy J. Mitra. 2014. Meta-representation of shape families. *ACM Trans. Graph.* 33, 4 (2014), 34:1–34:11. <https://doi.org/10.1145/2601097.2601185>
- Rao Fu, Cheng Wen, Qian Li, Xiao Xiao, and Pierre Alliez. 2023. BpNet: Bézier Primitive Segmentation on 3D Point Clouds. In *Proceedings of the Thirty-Second International Joint Conference on Artificial Intelligence, IJCAI 2023, 19th–25th August 2023, Macao, SAR, China*. ijcai.org, 754–762. <https://doi.org/10.24963/ijcai.2023/84>
- Haoxiang Guo, Shilin Liu, Hao Pan, Yang Liu, Xin Tong, and Baining Guo. 2022b. ComplexGen: CAD reconstruction by B-rep chain complex generation. *ACM Trans. Graph.* 41, 4 (2022), 129:1–129:18. <https://doi.org/10.1145/3528223.3530078>
- Hao-Xiang Guo, Yang Liu, Hao Pan, and Baining Guo. 2022a. Implicit Conversion of Manifold B-Rep Solids by Neural Halfspace Representation. *ACM Trans. Graph.* 41, 6 (2022), 276:1–276:15. <https://doi.org/10.1145/3550454.3555502>
- Karim Hamza and Kazuhiro Saitou. 2004. Optimization of Constructive Solid Geometry Via a Tree-Based Multi-objective Genetic Algorithm. In *Genetic and Evolutionary Computation - GECCO 2004, Genetic and Evolutionary Computation Conference, Seattle, WA, USA, June 26–30, 2004, Proceedings, Part II (Lecture Notes in Computer Science, Vol. 3103)*, Kalyanmoy Deb, Riccardo Poli, Wolfgang Banzhaf, Hans-Georg Beyer, Edmund K. Burke, Paul J. Darwen, Dipankar Dasgupta, Dario Floreano, James A. Foster, Mark Harman, Owen Holland, Pier Luca Lanzi, Lee Spector, Andrea Tettamanzi, Dirk Thierens, and Andrew M. Tyrrell (Eds.). Springer, 981–992. https://doi.org/10.1007/978-3-540-24855-2_110
- Kaiming He, Xinlei Chen, Saining Xie, Yanghao Li, Piotr Dollár, and Ross B. Girshick. 2022. Masked Autoencoders Are Scalable Vision Learners. In *IEEE/CVF Conference on Computer Vision and Pattern Recognition, CVPR 2022, New Orleans, LA, USA, June 18–24, 2022*. IEEE, 15979–15988. <https://doi.org/10.1109/CVPR52688.2022.01553>
- R. Kenny Jones, Homer Walke, and Daniel Ritchie. 2022. PLAD: Learning to Infer Shape Programs with Pseudo-Labels and Approximate Distributions. In *IEEE/CVF Conference on Computer Vision and Pattern Recognition, CVPR 2022, New Orleans, LA, USA, June 18–24, 2022*. IEEE, 9861–9870. <https://doi.org/10.1109/CVPR52688.2022.00964>
- Kacper Kania, Maciej Zieba, and Tomasz Kajdanowicz. 2020. UCSG-NET- Unsupervised Discovering of Constructive Solid Geometry Tree. In *Advances in Neural Information Processing Systems 33: Annual Conference on Neural Information Processing Systems 2020, NeurIPS 2020, December 6–12, 2020, virtual*, Hugo Larochelle, Marc’Aurelio Ranzato, Raia Hadsell, Maria-Florina Balcan, and Hsuan-Tien Lin (Eds.). <https://proceedings.neurips.cc/paper/2020/hash/63d5fb54a858dd033fe90e6e4a74b0f0-Abstract.html>
- Mohammad Sadil Khan, Elona Dupont, Sk Aziz Ali, Kseniya Cherenkova, Anis Kacem, and Djamilia Aouada. 2024. CAD-SIGNet: CAD Language Inference from Point Clouds using Layer-wise Sketch Instance Guided Attention. arXiv:2402.16768 [cs.CV]
- Vladimir G. Kim, Wilmot Li, Niloy J. Mitra, Siddhartha Chaudhuri, Stephen DiVerdi, and Thomas A. Funkhouser. 2013. Learning part-based templates from large collections of 3D shapes. *ACM Trans. Graph.* 32, 4 (2013), 70:1–70:12. <https://doi.org/10.1145/2461912.2461933>
- Alexander Kirillov, Eric Mintun, Nikhila Ravi, Hanzi Mao, Chloé Rolland, Laura Gustafson, Tete Xiao, Spencer Whitehead, Alexander C. Berg, Wan-Yen Lo, Piotr Dollár, and Ross B. Girshick. 2023. Segment Anything. In *IEEE/CVF International Conference on Computer Vision, ICCV 2023, Paris, France, October 1–6, 2023*. IEEE, 3992–4003. <https://doi.org/10.1109/ICCV51070.2023.00371>
- John F. Kolen and Stefan C. Kremer. 2001. *A field guide to dynamical recurrent networks*. John Wiley & Sons.
- David H. Laidlaw, W. Benjamin Trumbore, and John F. Hughes. 1986. Constructive solid geometry for polyhedral objects. In *Proceedings of the 13th Annual Conference on Computer Graphics and Interactive Techniques, SIGGRAPH 1986, Dallas, Texas, USA, August 18–22, 1986*, David C. Evans and Russell J. Athay (Eds.). ACM, 161–170. <https://doi.org/10.1145/15922.15904>
- Joseph George Lambourne, Karl D. D. Willis, Pradeep Kumar Jayaraman, Longfei Zhang, Aditya Sanghi, and Kamal Rahimi Malekshan. 2022. Reconstructing editable prismatic CAD from rounded voxel models. In *SIGGRAPH Asia 2022 Conference Papers, SA 2022, Daegu, Republic of Korea, December 6–9, 2022*, Soon Ki Jung, Jeehee Lee, and Adam W. Bargteil (Eds.). ACM, 53:1–53:9. <https://doi.org/10.1145/3550469.3555424>
- Lingxiao Li, Minhuk Sung, Anastasia Dubrovina, Li Yi, and Leonidas J. Guibas. 2019. Supervised Fitting of Geometric Primitives to 3D Point Clouds. In *IEEE Conference on Computer Vision and Pattern Recognition, CVPR 2019, Long Beach, CA, USA, June 16–20, 2019*. Computer Vision Foundation / IEEE, 2652–2660. <https://doi.org/10.1109/CVPR.2019.00276>
- Pu Li, Jianwei Guo, Xiaopeng Zhang, and Dong-Ming Yan. 2023a. SECAD-Net: Self-Supervised CAD Reconstruction by Learning Sketch-Extrude Operations. In *IEEE/CVF Conference on Computer Vision and Pattern Recognition, CVPR 2023, Vancouver, BC, Canada, June 17–24, 2023*. IEEE, 16816–16826. <https://doi.org/10.1109/CVPR52729.2023.01613>
- Yuanqi Li, Shun Liu, Xinran Yang, Jianwei Guo, Jie Guo, and Yanwen Guo. 2023b. Surface and Edge Detection for Primitive Fitting of Point Clouds. In *ACM SIGGRAPH 2023 Conference Proceedings, SIGGRAPH 2023, Los Angeles, CA, USA, August 6–10, 2023*, Erik Brunvand, Alla Sheffer, and Michael Wimmer (Eds.). ACM, 44:1–44:10. <https://doi.org/10.1145/3588432.3591522>
- Weijian Ma, Minyang Xu, Xueyang Li, and Xiangdong Zhou. 2023. MultiCAD: Contrastive Representation Learning for Multi-modal 3D Computer-Aided Design Models. In *Proceedings of the 32nd ACM International Conference on Information and Knowledge Management*. 1766–1776.
- Yatian Pang, Wenxiao Wang, Francis E. H. Tay, Wei Liu, Yonghong Tian, and Li Yuan. 2022. Masked Autoencoders for Point Cloud Self-supervised Learning. In *Computer Vision - ECCV 2022 - 17th European Conference, Tel Aviv, Israel, October 23–27, 2022, Proceedings, Part II (Lecture Notes in Computer Science, Vol. 13662)*, Shai Avidan, Gabriel J. Brostow, Moustapha Cissé, Giovanni Maria Farinella, and Tal Hassner (Eds.). Springer, 604–621. https://doi.org/10.1007/978-3-031-20086-1_35
- Jeong Joon Park, Peter R. Florence, Julian Straub, Richard A. Newcombe, and Steven Lovegrove. 2019. DeepSDF: Learning Continuous Signed Distance Functions for Shape Representation. In *IEEE Conference on Computer Vision and Pattern Recognition, CVPR 2019, Long Beach, CA, USA, June 16–20, 2019*. Computer Vision Foundation / IEEE, 165–174. <https://doi.org/10.1109/CVPR.2019.00025>
- Despoina Paschalidou, Ali Osman Ulusoy, and Andreas Geiger. 2019. Superquadrics Revisited: Learning 3D Shape Parsing Beyond Cuboids. In *IEEE Conference on Computer Vision and Pattern Recognition, CVPR 2019, Long Beach, CA, USA, June 16–20, 2019*. Computer Vision Foundation / IEEE, 10344–10353. <https://doi.org/10.1109/CVPR.2019.01059>
- Daxuan Ren, Jianmin Zheng, Jianfei Cai, Jiatong Li, Haiyong Jiang, Zhongang Cai, Junzhe Zhang, Liang Pan, Mingyuan Zhang, Haiyu Zhao, and Shuai Yi. 2021. CSG-Stump: A Learning Friendly CSG-Like Representation for Interpretable Shape Parsing. In *2021 IEEE/CVF International Conference on Computer Vision, ICCV 2021, Montreal, QC, Canada, October 10–17, 2021*. IEEE, 12458–12467. <https://doi.org/10.1109/ICCV48922.2021.01225>

- Daquan Ren, Jianmin Zheng, Jianfei Cai, Jiatong Li, and Junzhe Zhang. 2022. ExtrudeNet: Unsupervised Inverse Sketch-and-Extrude for Shape Parsing. In *Computer Vision - ECCV 2022 - 17th European Conference, Tel Aviv, Israel, October 23-27, 2022, Proceedings, Part II (Lecture Notes in Computer Science, Vol. 13662)*, Shai Avidan, Gabriel J. Brostow, Moustapha Cissé, Giovanni Maria Farinella, and Tal Hassner (Eds.). Springer, 482–498. https://doi.org/10.1007/978-3-031-20086-1_28
- Ruwen Schnabel, Roland Wahl, and Reinhard Klein. 2007. Efficient RANSAC for Point-Cloud Shape Detection. *Comput. Graph. Forum* 26, 2 (2007), 214–226. <https://doi.org/10.1111/J.1467-8659.2007.01016.X>
- Vadim Shapiro and Donald L. Vossler. 1991. Construction and optimization of CSG representations. *Comput. Aided Des.* 23, 1 (1991), 4–20. [https://doi.org/10.1016/0010-4485\(91\)90077-A](https://doi.org/10.1016/0010-4485(91)90077-A)
- Vadim Shapiro and Donald L. Vossler. 1993. Separation for Boundary to CSG Conversion. *ACM Trans. Graph.* 12, 1 (1993), 35–55. <https://doi.org/10.1145/169728.169723>
- Gopal Sharma, Rishabh Goyal, Difan Liu, Evangelos Kalogerakis, and Subhransu Maji. 2018. CSGNet: Neural Shape Parser for Constructive Solid Geometry. In *2018 IEEE Conference on Computer Vision and Pattern Recognition, CVPR 2018, Salt Lake City, UT, USA, June 18-22, 2018*. Computer Vision Foundation / IEEE Computer Society, 5515–5523. <https://doi.org/10.1109/CVPR.2018.00578>
- Gopal Sharma, Rishabh Goyal, Difan Liu, Evangelos Kalogerakis, and Subhransu Maji. 2022. Neural Shape Parsers for Constructive Solid Geometry. *IEEE Trans. Pattern Anal. Mach. Intell.* 44, 5 (2022), 2628–2640. <https://doi.org/10.1109/TPAMI.2020.3044749>
- Gopal Sharma, Difan Liu, Subhransu Maji, Evangelos Kalogerakis, Siddhartha Chaudhuri, and Radomir Mech. 2020. ParSeNet: A Parametric Surface Fitting Network for 3D Point Clouds. In *Computer Vision - ECCV 2020 - 16th European Conference, Glasgow, UK, August 23-28, 2020, Proceedings, Part VII (Lecture Notes in Computer Science, Vol. 12352)*, Andrea Vedaldi, Horst Bischof, Thomas Brox, and Jan-Michael Frahm (Eds.). Springer, 261–276. https://doi.org/10.1007/978-3-030-58571-6_16
- David Stutz. 2017. Learning Shape Completion from Bounding Boxes with CAD Shape Priors. <http://davidstutz.de/>
- David Stutz and Andreas Geiger. 2018. Learning 3D Shape Completion from Laser Scan Data with Weak Supervision. In *IEEE Conference on Computer Vision and Pattern Recognition (CVPR)*. IEEE Computer Society.
- Shubham Tulsiani, Hao Su, Leonidas J. Guibas, Alexei A. Efros, and Jitendra Malik. 2017. Learning shape abstractions by assembling volumetric primitives. In *Proceedings of the IEEE Conference on Computer Vision and Pattern Recognition*. 2635–2643.
- Mikaela Angelina Uy, Yen-Yu Chang, Minhyuk Sung, Purvi Goel, Joseph Lambourne, Tolga Birdal, and Leonidas J. Guibas. 2022. Point2Cyl: Reverse Engineering 3D Objects from Point Clouds to Extrusion Cylinders. In *IEEE/CVF Conference on Computer Vision and Pattern Recognition, CVPR 2022, New Orleans, LA, USA, June 18-24, 2022*. IEEE, 11840–11850. <https://doi.org/10.1109/CVPR52688.2022.01155>
- Haiping Wang, Yuan Liu, Qingyong Hu, Bing Wang, Jianguo Chen, Zhen Dong, Yulan Guo, Wenping Wang, and Bisheng Yang. 2023. Roreg: Pairwise point cloud registration with oriented descriptors and local rotations. *IEEE Transactions on Pattern Analysis and Machine Intelligence* (2023).
- Xiaogang Wang, Yuelang Xu, Kai Xu, Andrea Tagliasacchi, Bin Zhou, Ali Mahdavi-Amiri, and Hao Zhang. 2020. PIE-NET: Parametric Inference of Point Cloud Edges. In *Advances in Neural Information Processing Systems 33: Annual Conference on Neural Information Processing Systems 2020, NeurIPS 2020, December 6-12, 2020, virtual*, Hugo Larochelle, Marc’Aurelio Ranzato, Raia Hadsell, Maria-Florina Balcan, and Hsuan-Tien Lin (Eds.). <https://proceedings.neurips.cc/paper/2020/hash/e94550c93cd70fe748e6982b3439ad3b-Abstract.html>
- Karl D. D. Willis, Yewen Pu, Jieliang Luo, Hang Chu, Tao Du, Joseph G. Lambourne, Armando Solar-Lezama, and Wojciech Matusik. 2021. Fusion 360 gallery: a dataset and environment for programmatic CAD construction from human design sequences. *ACM Trans. Graph.* 40, 4 (2021), 54:1–54:24. <https://doi.org/10.1145/3450626.3459818>
- Q. Wu, K. Xu, and Jun Wang. 2018. Constructing 3D CSG Models from 3D Raw Point Clouds. *Comput. Graph. Forum* 37, 5 (2018), 221–232. <https://doi.org/10.1111/CGF.13504>
- Rundi Wu, Chang Xiao, and Changxi Zheng. 2021. DeepCAD: A Deep Generative Network for Computer-Aided Design Models. In *2021 IEEE/CVF International Conference on Computer Vision, ICCV 2021, Montreal, QC, Canada, October 10-17, 2021*. IEEE, 6752–6762. <https://doi.org/10.1109/ICCV48922.2021.00670>
- Xiang Xu, Pradeep Kumar Jayaraman, Joseph George Lambourne, Karl D. D. Willis, and Yasutaka Furukawa. 2023. Hierarchical Neural Coding for Controllable CAD Model Generation. In *International Conference on Machine Learning, ICML 2023, 23-29 July 2023, Honolulu, Hawaii, USA (Proceedings of Machine Learning Research, Vol. 202)*, Andreas Krause, Emma Brunskill, Kyunghyun Cho, Barbara Engelhardt, Sivan Sabato, and Jonathan Scarlett (Eds.). PMLR, 38443–38461. <https://proceedings.mlr.press/v202/xu23f.html>
- Xianghao Xu, Wenzhe Peng, Chin-Yi Cheng, Karl D. D. Willis, and Daniel Ritchie. 2021. Inferring CAD Modeling Sequences Using Zone Graphs. In *IEEE Conference on Computer Vision and Pattern Recognition, CVPR 2021, virtual, June 19-25, 2021*. Computer Vision Foundation / IEEE, 6062–6070. <https://doi.org/10.1109/CVPR46437.2021.00600>
- Xiang Xu, Karl DD Willis, Joseph G Lambourne, Chin-Yi Cheng, Pradeep Kumar Jayaraman, and Yasutaka Furukawa. 2022. SkexGen: Autoregressive Generation of CAD Construction Sequences with Disentangled Codebooks. In *International Conference on Machine Learning*. PMLR, 24698–24724.
- Siming Yan, Zhenpei Yang, Chongyang Ma, Haibin Huang, Etienne Vouga, and Qixing Huang. 2021. HPNet: Deep Primitive Segmentation Using Hybrid Representations. In *2021 IEEE/CVF International Conference on Computer Vision, ICCV 2021, Montreal, QC, Canada, October 10-17, 2021*. IEEE, 2733–2742. <https://doi.org/10.1109/ICCV48922.2021.00275>
- Fenggen Yu, Qimin Chen, Maham Tanveer, Ali Mahdavi-Amiri, and Hao Zhang. 2023. D²CSG: Unsupervised Learning of Compact CSG Trees with Dual Complements and Dropouts. In *Advances in Neural Information Processing Systems 36: Annual Conference on Neural Information Processing Systems 2023, NeurIPS 2023, New Orleans, LA, USA, December 10 - 16, 2023*, Alice Oh, Tristan Naumann, Amir Globerson, Kate Saenko, Moritz Hardt, and Sergey Levine (Eds.). http://papers.nips.cc/paper_files/paper/2023/hash/4732d425125832887f6c5a9675d49ead-Abstract-Conference.html
- Fenggen Yu, Zhiqin Chen, Manyi Li, Aditya Sanghi, Hooman Shayani, Ali Mahdavi-Amiri, and Hao Zhang. 2022. CAPRI-Net: Learning Compact CAD Shapes with Adaptive Primitive Assembly. In *IEEE/CVF Conference on Computer Vision and Pattern Recognition, CVPR 2022, New Orleans, LA, USA, June 18-24, 2022*. IEEE, 11758–11768. <https://doi.org/10.1109/CVPR52688.2022.01147>
- Xiangyu Zhu, Dong Du, Weikai Chen, Zhiyou Zhao, Yinyu Nie, and Xiaoguang Han. 2023. NerVE: Neural Volumetric Edges for Parametric Curve Extraction from Point Cloud. In *IEEE/CVF Conference on Computer Vision and Pattern Recognition, CVPR 2023, Vancouver, BC, Canada, June 17-24, 2023*. IEEE, 13601–13610. <https://doi.org/10.1109/CVPR52729.2023.01307>

A CAD DOMAIN-SPECIFIC LANGUAGE SEQUENCE

The domain-specific language (DSL) defined by SkexGen [Xu et al. 2022] contains the most frequently used CAD modeling operations, including curves {line, arc, circle}, feature operation {extrude}, and Boolean operation {union, subtraction}. Tab. 7 provides the overview of the tokens and parameters of the DSL in SkexGen [Xu et al. 2022]. SkexGen introduces a set of special tokens to denote different types of CAD modeling operations, where ϵ_* marks the end of “[operation type]”, e.g. ϵ_c, ϵ_e for the end of a curve and the end of extrusion. The parameters are supposed to be continuous and we follow previous works [Wu et al. 2021; Xu et al. 2023, 2022] to quantize them into discrete values to simplify the auto-regressive learning of the CAD DSL sequence. We have Eq. 9 for the quantization,

$$\mathbf{V} = \left\lfloor \frac{v - X_{\min}}{X_{\max} - X_{\min}} \times \mathbf{Q} \right\rfloor, \quad (9)$$

where v is the continuous value of a parameter, \mathbf{V} is its quantization counterpart. X_{\min} and X_{\max} are the range of v , $\lfloor \cdot \rfloor$ is Floor operation, \mathbf{Q} is the number of quantization bins of the $[X_{\min}, X_{\max}]$, i.e. to determine the number of divisions from X_{\min} to X_{\max} .

As a counterpart, we formulate the value dequantization as Eq. 10 to convert \mathbf{V} back to a continuous value,

$$\hat{v} = \mathbf{V} \times \frac{X_{\max} - X_{\min}}{\mathbf{Q}}, \quad (10)$$

where the \hat{v} is the dequantized approximation of v . The difference between \hat{v} and v is less than $\frac{X_{\max} - X_{\min}}{\mathbf{Q}}$.

The sketch part s is organized as a hierarchy of multiple curves that make up the normalized sketch. Specifically, s represents a “sketch-face-loop” hierarchy, in which a sketch can contain one or more faces, with a face being a 2D region bounded by loops. The loop is a closed path consisting of one or more curves. We use $\epsilon_s, \epsilon_f, \epsilon_l$ to represent the separation of hierarchical elements in s_{cur} . Different types of curves are uniformly noted as ϵ_c , identified by different numbers of curve parameters:

- Line–2 operation parameters, Start and End point.

Table 7. Description of CAD DSL tokens.

Operation	Token Type	Token Value Range	Description
Sketch	ε_s	1	End of a Sketch
	ε_f	2	End of a Face
	ε_l	3	End of a Loop
	ε_c	4	End of a Curve
	ε_x	[5, 68]	Curve
	ε_y	[5, 68]	Coordinates
Extrude	d^+	[2, 65]	Extruded Distance Towards Sketch Plane Normal
	d^-	[2, 65]	Extruded Distance Opposite Sketch Plane Normal
	τ_x	[2, 65]	Sketch Plane Origin
	τ_y	[2, 65]	
	τ_z	[2, 65]	
	θ	[2, 65]	
	ϕ	[2, 65]	Sketch Plane Orientation
	ρ	[2, 65]	Sketch Scaling Factor
	σ	[2, 65]	
	ε_e	1	End of an Extruding Parameters
Boolean Operations	β	{1, 0}	{Union, Subtraction}

- Arc-3 operation parameters, Start, Mid, and End point.
- Circle-4 operation parameters, 4 points that connect into mutual orthogonal diameters.

The curve parameters are 2D coordinates on the XY-axis and will be projected onto the sketch plane through the linear transformation derived from the extrude operation. In particular, given an arbitrary point on a curve $\vec{e} = (\varepsilon_x, \varepsilon_y, 0)^T$, the Euler angle (θ, ϕ, ρ) , the translation vector $\vec{t} = (\tau_x, \tau_y, \tau_z)^T$, and the scaling factor σ , the projected point \vec{e}_p is given by Eq. 11,

$$\vec{e}_p = \mathbf{R}_{xyz}(\theta, \phi, \rho)(\sigma \cdot \vec{e}) + \vec{t} \quad (11)$$

where $\mathbf{R}_{xyz}(\theta, \phi, \rho) \in \mathcal{SO}(3)$ combines the Euler angles in a rotation matrix in the orthogonal group $\mathcal{SO}(3)$.

B POINT CLOUD ENCODER

We implement the Point-MAE [He et al. 2022] encoder to extract point cloud features. Specifically, the input point cloud is first divided into irregular point patches p_{fps} via Farthest Point Sampling (FPS) and K-Nearest Neighborhood (KNN) retrieval. Formally, we have:

$$\begin{aligned} p_{\text{fps}} &= \text{FPS}(p_{\text{in}}), \quad p_{\text{in}} \in \mathbb{R}^{N_p \times 3}, \quad p_{\text{fps}} \in \mathbb{R}^{N_f \times 3}, \\ p_{\text{knn}} &= \text{KNN}(p_{\text{fps}}, p_{\text{in}}), \quad p_{\text{knn}} \in \mathbb{R}^{N_f \times k \times 3}, \end{aligned} \quad (12)$$

where p_{in} is the input point cloud, FPS samples points p_{fps} as centers of N_f point patches, and KNN selects k nearest points from p_{in} for each point patch. The embedding of the point patch is calculated as:

$$\begin{aligned} p_{\text{knn}} &= p_{\text{knn}} - p_{\text{fps}} \\ f_{\text{knn}} &= \text{PointNet}(p_{\text{knn}}) + \text{PE}(p_{\text{fps}}), \quad f_{\text{knn}} \in \mathbb{R}^{N_f \times C}, \end{aligned} \quad (13)$$

where PointNet is a lightweight MLP+max-pooling layer, and PE is a learnable positional embedding also implemented as an MLP layer. C is the number of feature channels. f_{knn} is then fed into a standard transformer. Each transformer block is implemented as a multi-head self-attention (SA) + MLP layer. The positional embedding $\text{PE}(p_{\text{fps}})$ is added to each block to provide point position information. The output of the transformer is the features of point cloud p_{in} , denoted as $f_{\text{in}} \in \mathbb{R}^{N_f \times C}$. To balance cost and performance, we set $k = 32$ in KNN, $N_p = 8192$, $N_f = 384$, $C = 384$. The number of transformer blocks is set as 6.

C POINT CLOUD SEGMENTATION NETWORK

We train a segmentation network to compare the differing regions between p_{full} and p_{prev} . The point cloud segmentation network consists of the Point-MAE encoder, a decoder, and a mask prediction head. The Decoder adopts three Transformer blocks and takes the concatenation of point cloud features $f_{\text{full}}, f_{\text{prev}}$ as input and outputs the features $f_{\text{mask}} \in \mathbb{R}^{2M \times C}$ which is fed to the mask prediction head. The mask prediction head is implemented as a fully connected layer to project f_{mask} to a point cloud mask \mathcal{M} . Then followed by a reshape and sigmoid, the segmentation mask \mathcal{M} is obtained as follows:

$$\mathcal{M} = \text{Sigmoid}(\text{Reshape}(\text{FC}(f_{\text{mask}}))), \quad \mathcal{M} \in \mathbb{R}^{2(N_f \times k) \times 1}. \quad (14)$$

The first N_p masks in \mathcal{M} are for the differing regions of p_{full} w.r.t. p_{prev} while the next N_p masks are for the differing region of p_{prev} w.r.t. p_{full} . We employ the binary cross-entropy loss to optimize the point cloud segmentation network.

Discussion. There are various applicable techniques to obtain the differing regions between p_{full} and p_{prev} . For example, a potential approach is first to perform point cloud registration on p_{full} and p_{prev} to align two point clouds. Followed by calculating the minimum Euclidean distance of each point in one point cloud to the other, we retain those points with distances exceeding a certain threshold. We believe that employing an advanced point cloud registration framework (e.g. [Wang et al. 2023]) allows us to obtain more precise inputs for our sequence reconstruction network, which we leave for future work.

D SINGLE-STEP RECONSTRUCTION AND SELECTION

D.1 Differentiable 3D Bounding Box Construction

In this section, we first introduce how to construct a 3D bounding box using parameters in a single-step sketch-extrude sequence o_t . Then we introduce how to construct the 3D bounding box in a differentiable way using the output of the sketch decoder (s-dec) and extrude decoder (e-dec).

Executing a single-step sketch-extrude sequence constructs an extrusion cylinder by extruding a sketch on the sketch plane. By

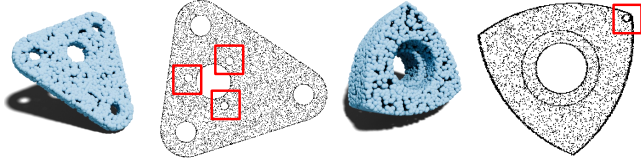


Fig. 17. The detailed structure of two point clouds from Fig. 9. There are some holes framed by a red box. Best viewed by zooming in.

replacing the sketch with its bounding box, the execution can construct the 3D bounding box of the extrusion cylinder while ensuring a differentiable process w.r.t. extruding parameters and sketch parameters. We first calculate the 2D bounding box of a sketch by calculating the maximal and minimal values along the x/y axis. Given a point representing one corner of the sketch bounding box $\vec{e}^l = (\varepsilon_x^l, \varepsilon_y^l, 0)^T$ and the extruded distance d^+, d^- , we apply Eq. 11 with a slight modification to project \vec{e}^l to two corresponding corners of the 3D bounding box as follows:

$$\begin{aligned}\vec{e}_p^{l1} &= \mathbf{R}_{xyz}(\theta, \phi, \rho)(\sigma \cdot \vec{e}^l + (0, 0, d^+)^T) + \vec{\tau}, \\ \vec{e}_p^{l2} &= \mathbf{R}_{xyz}(\theta, \phi, \rho)(\sigma \cdot \vec{e}^l + (0, 0, d^-)^T) + \vec{\tau}.\end{aligned}\quad (15)$$

Referring to Eq. 4, the output of s -dec and e -dec is the softmax token probability, requiring a non-differentiable arg max operator to convert them into token values. We instead calculate a differential sketch/extrude parameter by accumulating the token probability along all possible token values with their dot products. The calculation for the parameter at index h of the s -dec output is formatted as follows:

$$s^h = \sum_{j=0}^{Q_s-1} s^h \times j, \quad (16)$$

where $[0, Q_s - 1]$ is the value range of token s^h , and j is the component index of the output probability $s\text{-dec}(\cdot, \cdot)$, within a range of $[0, Q_s - 1]$. Once all tokens of s are calculated, the coordinates of sketch parameters can be obtained through dequantization Eq. 10. We select the minimum and maximum coordinates to form the corner of the sketch bounding box. Without loss of generality, extruding parameters of an output of the e -dec can be obtained in the same way.

Finally, by combining the above designs in Eq. 16, 10, 15, we can construct the 3D bounding box of the executed shape of a single-step sketch-extrude sequence in a differentiable way, leading to the $\text{bbox}(\cdot)$ operator in Eq. 5.

D.2 Training implementation

Training sample. Our raw training data comes from DeepCAD [Wu et al. 2021], where each data item contains a CAD model and one corresponding CAD modeling sequence. The CAD model is obtained by progressively executing the CAD modeling sequence just like Fig. 1. We sample p_{full} from the CAD model and p_{prev} can be sampled from the intermediate executions. Supposing that a CAD modeling sequence has N_O CAD modeling steps, p_{prev} for the first step is an empty point cloud and is identical to p_{full} at the final step.

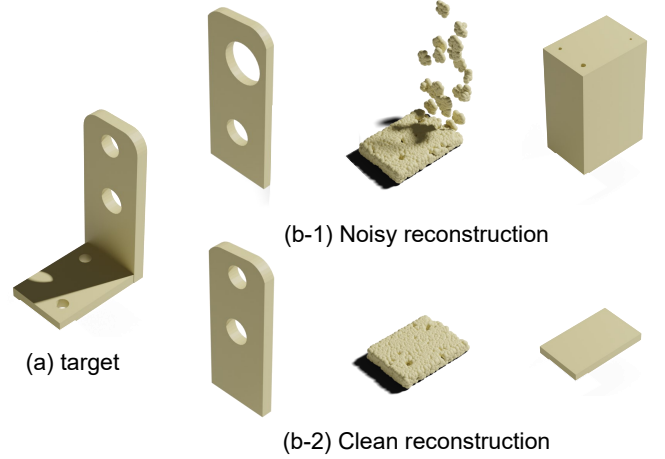


Fig. 18. Influence of accumulated noises during CAD modeling. (a) The ground truth 3D shape; (b) reconstruction of previous steps, remaining inputs not yet reconstructed, and reconstruction of the current step. We show results of inaccurate reconstruction of previous steps (b-1) and that of accurate ones (b-2).

Data augmentation. We also notice there are inevitable noises gradually accumulated during the iterative reconstruction, mainly introduced by imperfect point cloud segmentation mask $\mathcal{M}_{\text{full}}$ and $\mathcal{M}_{\text{prev}}$ and imprecise sequence reconstruction o_t . Imperfect $\mathcal{M}_{\text{full}}$ and $\mathcal{M}_{\text{prev}}$ leads to outliers or detail losses of a point cloud, while imprecise sequence parameters, e.g., Sketch Plane Origin (τ_x, τ_y, τ_z) in Extruding operations, will induce uncertainty for the executed shape of successive steps. They can deteriorate the performance by interfering with the quality of f_{ref} and prompt sampling. Even worse, noise accumulation may lead to reconstruction failure, as depicted in Fig. 18.

To mitigate the adverse effects of noises, we employ data augmentation to inject noises into training samples, making the network training more robust. Specifically, the noise of training samples is induced in the $\mathcal{M}_{\text{full}}$ and $\mathcal{M}_{\text{prev}}$ and training prompts. Noises introduced into p_{ref} can be controlled by \mathcal{M} , and we randomly invert $\mathcal{M}_{\text{full}}$ or $\mathcal{M}_{\text{prev}}$ with a probability of 5%. Second, training prompts sampled from sketch planes are scaled with a factor ranging from $[0.8, 1.1]$. In this way, prompts can adapt to noisy inputs not perfectly aligned with the ground-truth sketch plane.